



Timelike boundary and corner terms in the causal set action

Fay Dowker^{1,2} , Roger Liu^{1,3,*}  and Daniel Lloyd-Jones^{1,4} 

¹ Blackett Laboratory, Imperial College, Prince Consort Road, London SW7 2AZ, United Kingdom

² Perimeter Institute, 31 Caroline Street North, Waterloo, ON N2L 2Y5, Canada

³ Mathematical Institute, University of Oxford, Woodstock Road, Oxford OX2 6GG, United Kingdom

⁴ Department of Applied Mathematics and Theoretical Physics, University of Cambridge, Wilberforce Road, Cambridge CB3 0WA, United Kingdom

E-mail: xiaodi.liu@wadham.ox.ac.uk, f.dowker@imperial.ac.uk and dl738@cam.ac.uk

Received 30 April 2025; revised 23 September 2025

Accepted for publication 25 September 2025

Published 13 October 2025



CrossMark

Abstract

The causal set action of dimension d is investigated for causal sets that are Poisson sprinklings into manifolds that are regions of d -dimensional Minkowski space. Evidence, both analytic and numerical, is provided for the conjecture that as the discreteness length l tends to zero, the mean of the causal set action over Poisson sprinklings into a manifold with a timelike boundary, is dominated by a term proportional to the volume of the timelike boundary and diverges like l^{-1} . A novel conjecture for the contribution to the causal set action from co-dimension two corners, also known as joints, is proposed and justified.

Keywords: quantum gravity, causal sets, action, boundary terms

* Author to whom any correspondence should be addressed.



Original Content from this work may be used under the terms of the [Creative Commons Attribution 4.0 licence](https://creativecommons.org/licenses/by/4.0/). Any further distribution of this work must maintain attribution to the author(s) and the title of the work, journal citation and DOI.

Contents

1. Introduction	3
2. The causal set action	4
2.1. The discrete-continuum correspondence for causal sets	4
2.2. The BDG action	5
2.3. Mean of the action	6
2.4. Regimes	7
2.5. Conjectures	8
2.6. Weighted integral method in flat space	9
2.7. Smearing to tame the fluctuations	10
3. Timelike boundaries in 1+1 dimensions	11
3.1. Triangle in 1+1	11
3.2. 1+1 Infinite t	12
4. d -dimensional infinite slab in the embedded regime	14
4.1. Set-up	14
4.2. Extending the triangle	15
4.3. Results	16
5. Simulations of timelike boundaries	16
5.1. Simulation of $d = 3$ ball in embedded regime	16
5.1.1. Results	17
5.2. Simulation of $d = 3$ cube, isolated	18
6. Holes	19
6.1. Isolated annulus	19
6.1.1. Region 1 to 8	20
6.1.2. Region 1 to 6	21
6.1.3. Full result	22
6.1.4. Simulations	22
6.2. Spacelike holes	22
6.3. Timelike holes	25
7. Spacelike joints	26
7.1. The Lozenge	26
7.2. Lorentzian angle	29
7.3. Spacelike triangle	29
7.4. Higher dimensions	31
8. Discussion	33
Data availability statement	35
Acknowledgment	35
Appendix A. Causal set actions for specific dimensions	35
Appendix B. The cross terms in the $d = 2$ diamond	36
Appendix C. $d = 2$ timelike-spacelike (t-s) corners in the embedded regime	37
C.1. Half lozenge	37
C.2. Lorentzian angle	38
C.3. Quarter lozenge	39
Appendix D. Argument for assumption	40
D.1. Integration in $A(\text{up})$	42
D.2. Integration in $A(\text{down})$	42
References	43

1. Introduction

In the causal set approach to quantum gravity, a major direction in constructing a quantum dynamics for causal sets is what might be called *state sum models* in which the heuristic of the continuum gravitational path integral over manifolds and geometries,

$$Z(V) = \sum_{M \in \mathcal{M}} \int_{g \in \mathcal{G}} [dg] e^{iS(g)/\hbar}, \quad (1)$$

is interpreted as being fundamentally a path *sum*, Z , given by:

$$Z(n) = \sum_{\mathcal{C} \in \Omega_n} e^{iS(\mathcal{C})/\hbar} \quad (2)$$

where Ω_n is some collection of (order isomorphism classes of) causal sets of cardinality n [1, 2]. The model is defined by Ω_n and by the action $S(\mathcal{C})$ and there may be a symmetry factor such as $1/|\text{Aut}(\mathcal{C})|$ where $\text{Aut}(\mathcal{C})$ is the group of automorphisms of \mathcal{C} ⁵.

The best studied candidates for the action of a causal set are the members of the Benincasa–Dowker–Glaser (BDG) family of actions [6–9]. These causal set actions and their smeared versions will be defined in the next section. The discreteness of causal sets not only means that the gravitational path integral becomes a path sum but, when the sum is restricted to causal sets of a fixed cardinality as above, the sum is actually finite and concerns about mathematical existence and convergence of the path integral are alleviated. This finiteness is one of the original motivations for causal set theory [10].

In order to recover physics as we currently understand it, the path sum would have to exhibit a continuum regime in which some version of general relativity (GR) emerges. A necessary condition for this to happen is that the non-manifoldlike causal sets—i.e. causal sets that are not approximated by any continuum Lorentzian spacetime—should be suppressed in the sum over causal sets. There is mounting evidence that the BDG action can do the job of suppressing certain classes of non-manifoldlike causal sets in the sum. One important such class of non-manifoldlike causal sets is the Kleitman–Rothschild (KR) orders. These causal sets only have 3 layers, representing universes that, roughly speaking, last only 3 Planck times and so are clearly non-manifoldlike. However, the KR orders are the most numerous causal sets: the ratio between the number of KR orders of cardinality n and the number of causal sets of cardinality n tends to 1 as n tends to infinity [11, 12]. However, this entropic catastrophe is averted for the KR orders which are shown to be strongly suppressed in the path sum by the BDG action [13] and further work extends this to other actions and other classes of non-manifoldlike causal sets [14–16].

A second necessary condition for GR to be recovered from the path sum is that causal sets that are well-approximated by continuum Lorentzian spacetimes that are not ‘GR solutions’ should be suppressed in the sum, relative to those that are approximated by GR solutions. This condition has at least two different aspects. One aspect is the suppression of causal sets corresponding to non-solutions of the Einstein equations relative to solutions of the Einstein equations⁶, which include matter in cases where it is present. For this reason the action of

⁵ Another direction in the quest for a quantum dynamics for causal sets is to generalise the classical sequential growth models of Rideout and Sorkin [3] and to construct the decoherence functional or double path integral of a quantum measure theory for a growing causal set [4, 5].

⁶ By solution of the Einstein equations we mean a metric and matter configuration that together extremize the total action which is the sum of the Einstein–Hilbert (EH) action for the metric and the action for the matter in the theory.

a manifoldlike causal set should approximate the EH action so that the usual Feynmannian stationary phase argument may be invoked [17]:

‘Suppose that for all paths, S is very large compared to \hbar . One path contributes a certain amplitude. For a nearby path, the phase is quite different, because with an enormous S even a small change in S means a completely different phase—because \hbar is so tiny. So nearby paths will normally cancel their effects out in taking the sum—except for one region, and that is when a path and a nearby path all give the same phase in the first approximation (more precisely, the same action within \hbar). Only those paths will be the important ones.’

The second aspect is the related question of what extra conditions, in addition to being a solution of the Einstein equations, a Lorentzian geometry should satisfy to be considered a ‘GR solution’.

For example, a broad class of possible ‘extra conditions’ are the various causality conditions on spacetime such as strong causality or global hyperbolicity. We expect that quantum gravity when we have it will tell us what the physical axioms of GR actually are. Quantum gravity may rule out certain classes of spacetimes even though they are, formally, solutions of the Einstein equations. An immediate example of this is the ruling out of spacetimes with closed timelike curves (CTCs) from causal set quantum gravity: a Lorentzian geometry with CTCs cannot approximate any causal set and so cannot emerge as a prediction from a sum-over-causal-sets.

In this work we investigate properties of the BDG causal set action with an eye to the question of which solutions of the vacuum Einstein equations may be favoured over which other solutions of the vacuum Einstein equations by a causal set sum-over-histories. We consider only finite volume flat spacetimes and so they are all, formally, solutions of the vacuum Einstein equations but they will differ in their shapes, causal properties and boundary properties.

The paper is structured as follows: section 2 covers the foundations of causal set theory, including the BDG action and the conjectures surrounding this action, along with the analytic and computational techniques used in this paper to calculate the action. In section 3, we present analytic results for the mean causal set action for manifolds with timelike boundaries in $1+1$ dimensions. This is extended in section 4 for manifolds with timelike boundaries in arbitrary dimensions analytically. In section 5, the mean action for manifolds with timelike boundaries is found computationally. We then move onto another class of manifolds in section 6, those with holes, using both analytic and computational techniques, resulting in a new conjecture. Finally, section 7 presents analytic results for the mean causal set action of manifolds with spacelike corners, known as joints, using which we modify a conjecture.

2. The causal set action

2.1. The discrete-continuum correspondence for causal sets

A causal set (\mathcal{C}, \prec) is well-approximated by a d -dimensional Lorentzian manifold (M, g) at length scale l if there is a *faithful embedding* of (\mathcal{C}, \prec) in (M, g) at density $\rho = l^{-d}$ [10]. For more details about this criterion see [10] and section 3.2 of [18]. In the causal set literature it is widely assumed that a causal set (\mathcal{C}, \prec) is faithfully embeddable in Lorentzian manifold (M, g) if and only if (\mathcal{C}, \prec) is a *typical outcome* of a Poisson point process in (M, g) of density $\rho = l^{-1}$ [10]. This process is known as sprinkling and an outcome of the process is referred to

as a sprinkling or as a sprinkled causal set ⁷. For the purposes of this paper we will follow the literature that assumes manifoldlikeness for a causal set is equivalent to the causal set being a typical Poisson sprinkling ⁸.

There is growing evidence that the discrete-continuum correspondence described above works, namely that a typical sprinkled causal set is indeed rich enough to encode all the geometric information of the Lorentzian geometry on scales large compared to the discreteness scale set by the density. Much of the evidence is of the following form. Let $\mathcal{G}(M, g)$ be a geometric or topological property of the Lorentzian manifold (M, g) for which we are able, somehow or other, to glean a causal set analogue $G(\mathcal{C}, \prec)$ which is a function of a causal set (any causal set) (\mathcal{C}, \prec) . By Poisson sprinkling the manifold at density ρ and evaluating G on the random sprinkled causal set, G becomes a random variable $\mathbf{G}(M, g, \rho)$ depending on the Lorentzian geometry and the density. If a typical value of \mathbf{G} is close to the continuum geometric quantity \mathcal{G} then a typical sprinkled causal set indeed encodes that geometric quantity.

Therefore, with a proposed causal set geometric property G in hand, one first computes the mean, $\langle \mathbf{G} \rangle$ of \mathbf{G} in the sprinkling process in the limit as ρ the sprinkling density tends to infinity. If this gives the correct continuum quantity $\mathcal{G}(M)$ then we are in business and the next task becomes one of working out i) the finite ρ correction to the limiting value to show it is small for large enough ρ and ii) the fluctuations around the mean to show they are small so that the value of G for a typical sprinkling at Planckian density is close to the continuum value.

There is a growing list of proposals for causal set analogues of continuum geometric quantities [20, 21]. Some proposals are only verified to work in regions of Minkowski space and some are verified to have the correct mean over sprinklings but yet lack a proper investigation of the fluctuations around the mean.

2.2. The BDG action

The Ricci scalar curvature is a geometric quantity with a causal set analogue and summing the scalar curvature analogue over the whole causal set gives the BDG 1-parameter family of actions for a causal set \mathcal{C} [6–9]:

$$\frac{1}{\hbar} S^{(d)}(\mathcal{C}) = -\alpha_d \left(\frac{l}{l_p} \right)^{d-2} \left(N + \frac{\beta_d}{\alpha_d} \sum_{i=1}^{n_d} C_i^{(d)} N_i \right), \quad (3)$$

where $l_p := (8\pi G\hbar)^{1/d-2}$ is the Planck length in d dimensions, α_d , β_d and $C_i^{(d)}$ are known, dimension dependent constants of order one and $n_d = \lfloor d/2 \rfloor + 2$. For fixed d , the $C_i^{(d)}$ constants alternate in sign with i . The values of these constants are given in [9]. l is the *fundamental length* in the theory and it is expected to be of order the Planck length so that the factor $(l/l_p)^{d-2}$ in the action is a dimensionless constant of order 1. N is the cardinality of the causal set \mathcal{C} and N_i is the number of pairs of elements a, b such that $|[a, b]| = i - 1$, where $[a, b] = \{c \in \mathcal{C} | a \prec c \prec b\}$, in other words, N_i is the number of exclusive order intervals of cardinality $i - 1$ [22]. It is important to notice that N_i is a ‘‘bilocal’’ quantity: we can write it explicitly in the form

$$N_i = \sum_{x \in \mathcal{C}} \sum_{y \in \mathcal{C}} \chi(x, y) \quad (4)$$

⁷ Strictly, the outcome of the sprinkling process is a causal set (\mathcal{C}, \prec) together with its embedding in (M, g) . It should be clear in context whether ‘sprinkled causal set’ refers to the causal set only or refers to the set and its embedding.

⁸ For discussion about the relationship between faithful embedding and Poisson sprinkling see [19].

where $\chi(x, y)$ is a characteristic function depending on 2 elements of the causal set,

$$\chi(x, y) = \begin{cases} 1, & |[x, y]| = i - 1 \\ 0, & \text{else.} \end{cases} \quad (5)$$

This bilocal nature of the causal set action implies that, for subcausets A and B in a causal set \mathcal{C} we have $S^{(d)}(A \cup B) \neq S^{(d)}(A) + S^{(d)}(B) - S^{(d)}(A \cap B)$ because of bilocal contributions from order intervals that begin in one subcauset and end in the other. For subcausets A and B of a causal set \mathcal{C} , we can define a more general ‘bi-action’ [7]:

$$\frac{1}{\hbar} S^{(d)}(\mathcal{C}; A, B) = -\alpha_d \left(\frac{l}{l_p} \right)^{d-2} \left(N[A, B] + \frac{\beta_d}{\alpha_d} \sum_{i=1}^{n_d} C_i^{(d)} N_i[A, B] \right), \quad (6)$$

where $N[A, B] = |A \cap B|$, and $N_i[A, B]$ is the number of pairs of elements a, b such that $a \in A$ and $b \in B$ and $|[b, a]| = i - 1$. In other words $N_i[A, B]$ is the number of order intervals of cardinality $i - 1$ such that the minimal element is in B and the maximal element is in A . We note that $S(\mathcal{C}; \mathcal{C}, \mathcal{C}) = S(\mathcal{C})$.

The explicit forms of equation (3) for $d = 2, 3, 4$ are listed in appendix A.

2.3. Mean of the action

Henceforth, for brevity we will refer to a Lorentzian manifold (M, g) just as M and a causal set (\mathcal{C}, \prec) as \mathcal{C} and will consider only sprinkled causal sets. We will assume that M is of dimension d that matches the action we calculate.

As described above, evaluating the d -action (3) of a causal set sprinkled in a manifold M of dimension d and finite volume V turns N, N_i and the action S itself into random variables, \mathbf{N}, \mathbf{N}_i and $\mathbf{S}^{(d)}$ that each depend on M and on the density of sprinkling ρ . For example $\langle \mathbf{N} \rangle = \rho V$. We will refer to $\mathbf{S}^{(d)}$ as the random action of M and taking the mean of the random action over sprinklings gives [22]

$$\begin{aligned} \frac{1}{\hbar} \langle \mathbf{S}_\rho^{(d)}(M) \rangle &= -\alpha_d \left(\frac{l}{l_p} \right)^{d-2} \left(\langle \mathbf{N}_\rho^{(d)}(M) \rangle + \frac{\beta_d}{\alpha_d} \sum_{i=1}^{n_d} C_i^{(d)} \langle \mathbf{N}_{i,\rho}^{(d)}(M) \rangle \right) \\ &= -\alpha_d \left(\frac{l}{l_p} \right)^{d-2} \left(\rho V + \frac{\beta_d}{\alpha_d} \sum_{i=1}^{n_d} C_i^{(d)} \rho^2 \int_M dV_x \int_{M \cap J^+(x)} dV_y \frac{(\rho V_{xy})^{i-1} e^{-\rho V_{xy}}}{(i-1)!} \right) \end{aligned} \quad (7)$$

where V_{xy} is the volume of the causal interval between points x and y . $dV_x = d^d x \sqrt{-g(x)}$ and likewise for dV_y . The origin of the integral expression in the second line is the Poissonian probability of exactly $i - 1$ points being sprinkled in the causal interval of volume V_{xy} between x and y . This expression can be written more compactly in terms of a differential operator $\hat{\mathcal{O}}_d$ [22]:

$$\begin{aligned} \frac{1}{\hbar} \langle \mathbf{S}_\rho^{(d)}(M) \rangle &= -\alpha_d \left(\frac{l}{l_p} \right)^{d-2} \left(\rho V + \frac{\beta_d}{\alpha_d} \rho^2 \hat{\mathcal{O}}_d X_\rho \right) \\ X_\rho &= \int_M dV_x \int_{M \cap J^+(x)} dV_y e^{-\rho V_{xy}}, \\ \hat{\mathcal{O}}_d &= \sum_{i=1}^{n_d} C_i^{(d)} \frac{\rho^{i-1}}{(i-1)!} \left(-\frac{d}{d\rho} \right)^{i-1}. \end{aligned} \quad (8)$$

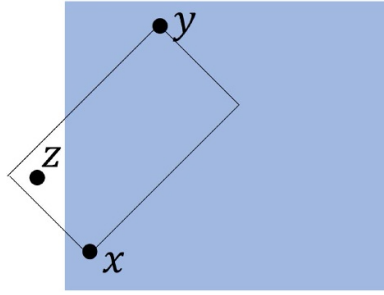


Figure 1. As an example, the blue region is M , a non-causally convex manifold. x, y are elements of \mathcal{C} but z is an element only of $\tilde{\mathcal{C}}$. Whether the order interval $[x, y]$ counts as having cardinality 0 or 1 depends on whether we are working in the isolated or embedded regime, respectively.

If we partition a manifold M into the union of two non-intersecting regions X and Y , and sprinkle into M with subcauset A in region X and subcauset B in Y , we can similarly turn the bi-action (6) into a random variable, $\mathcal{S}_\rho^{(d)}(M; X, Y)$.

In this case, the mean of the action for the entire manifold can then be calculated using:

$$\langle \mathcal{S}_M \rangle = \langle \mathcal{S}_X \rangle + \langle \mathcal{S}_Y \rangle + \langle \mathcal{S}_{X,Y} \rangle + \langle \mathcal{S}_{Y,X} \rangle \tag{9}$$

where the shorthand $\mathcal{S}_M = \mathcal{S}_\rho^{(d)}(M)$ and $\mathcal{S}_{X,Y} = \mathcal{S}_\rho^{(d)}(M; X, Y)$ have been used. This can be generalised if the manifold is partitioned into more regions: the action is the sum of the actions for each element of the partition plus bi-action cross terms between all ordered pairs of elements of the partition.

2.4. Regimes

In all the cases we consider in this paper the manifold we sprinkle into, M , is a finite region of Minkowski spacetime \mathbb{M}^d . When we sprinkle into a manifold M that is a submanifold of a larger manifold \tilde{M} , we can consider the sprinkled causal set \mathcal{C} to be a subset of $\tilde{\mathcal{C}}$ where $\tilde{\mathcal{C}}$ is the sprinkling in \tilde{M} . This can have consequences for the calculation of the action of \mathcal{C} depending on whether or not M is *causally convex* in \tilde{M} :

Definition . M is *causally convex* in \tilde{M} if, for any 2 points in M , the causal interval between these 2 points in \tilde{M} is contained in M .

In the BDG action (3), calculating N_i involves counting the number of causal set elements in the order interval between 2 elements. If M is not causally convex, when evaluating the action of \mathcal{C} we must decide whether or not to include elements sprinkled in the larger manifold $\tilde{M} = \mathbb{M}^d$.

If M is not causally convex we must decide between two different *regimes* [23]:

1. The isolated regime: the causal set \mathcal{C} and manifold M are considered to be physical spacetimes in and of themselves. For example, in figure 1, M is the blue rectangle and the sprinkled point z does not exist so $|[x, y]| = 0$ and the pair (x, y) is counted in N_1 . In the integral for the mean of the action, the area V_{xy} equals the area of the diamond between x and y intersected with M .

2. The embedded regime: the manifold M is a sub-manifold embedded within the larger manifold \tilde{M} and causal set \mathcal{C} is a subset of $\tilde{\mathcal{C}}$. Point z in figure 1 lies in this larger manifold and so is included in the order interval between x and y . As a result, $[[x, y]] = 1$ and the pair (x, y) is counted in N_2 . V_{xy} is the area of the full diamond.

The isolated regime is more relevant to our purpose of investigating the actions of causal sets corresponding to manifolds with different boundary properties and understanding how they contribute to the sum-over-histories. However, the embedded regime sometimes allows analytic results to be obtained because the volume V_{xy} is simpler and so we will also investigate the action in the embedded regime. In most cases, we find that the two regimes give similar results.

2.5. Conjectures

For globally hyperbolic manifolds, in the limit ρ tends to infinity, the mean of the random action was conjectured to be local and to equal the EH action plus a boundary term [7]:

Conjecture 1.

$$\lim_{\rho \rightarrow \infty} \frac{1}{\hbar} \langle S_\rho^{(d)}(M) \rangle = \frac{1}{l_p^{d-2}} \int_M d^d x \sqrt{-g} \frac{R}{2} + \frac{1}{l_p^{d-2}} \text{Vol}_{d-2}(J). \quad (10)$$

$\text{Vol}_{d-2}(J)$ is the volume of the so-called *joint*. A joint is a co-dimension 2 surface that is the intersection of the the future boundary and the past boundary of the spacetime, where the future (past) boundary is the set of points where future directed causal curves in M leave M . (10) has been proved for causal diamonds in Minkowski space in any dimension [24]: for example, for $d = 2$ the volume of the joint is 2, there is no Planck length and the limit of the mean of the action equals 2. Further evidence has been provided for the conjecture in the case of causal intervals and other regions in curved spacetime with low curvature [22, 25].

However, conjecture 1 had not been investigated for joints between 2 spacelike boundaries and in section 7 we will show that the joint term in the conjecture above is not correct in general and must be modified to:

Conjecture 1':

$$\lim_{\rho \rightarrow \infty} \frac{1}{\hbar} \langle S_\rho^{(d)}(M) \rangle = \frac{1}{l_p^{d-2}} \int_M d^d x \sqrt{-g} \frac{R}{2} + \frac{1}{l_p^{d-2}} \int_J d\mu(\lambda) \coth(\theta(\lambda)). \quad (11)$$

where $\theta(\lambda)$ is the Lorentzian angle between the tangent vectors to the past and future boundaries respectively at the point λ on the joint and $d\mu(\lambda)$ is the $(d-2)$ -dimensional volume measure on the joint. This is consistent with conjecture 1 in the cases in which conjecture 1 was tested because in those cases θ is constant and equal to infinity and so $\coth(\theta) = 1$.

For manifolds with timelike boundaries (an example of non-globally hyperbolic manifolds), the conjecture is [7]:

Conjecture 2.

$$\lim_{\rho \rightarrow \infty} \frac{1}{\hbar} \langle S_\rho^{(d)}(M) \rangle \rho^{-1/d} = \frac{1}{l_p^{d-2}} a_d^{\text{emb/iso}} \text{Vol}_{d-1}(T) \quad (12)$$

where $a_d^{\text{emb/iso}}$ is a d -dependent dimensionless coefficient, different according to whether the action is calculated in the embedded or isolated regime, and $\text{Vol}_{d-1}(T)$ is the volume of the timelike boundary T . This implies that the mean of the random action diverges like $\rho^{1/d} = l^{-1}$

as the discreteness scale l goes to zero. In the sum-over-histories, then, such causal sets will have very large actions, with potential consequences that we will discuss in the final section. For $d=2$, these conjectures were first investigated numerically in [26] and have been tested on a rectangle and a disc in [23], and the coefficients found to be:

$$\begin{aligned} a_2^{\text{emb}} &= \frac{1}{2} \sqrt{\frac{\pi}{2}} \\ a_2^{\text{iso}} &= 0.6959. \end{aligned} \tag{13}$$

a_2^{iso} is a value calculated from numerical integrations and there is no error estimation [23].

2.6. Weighted integral method in flat space

To compute the mean of the action (equation (7)) in flat spacetime ($dV_x = d^d x$), we must evaluate the integral X_ρ from equation (8). A way of calculating this integral in the embedded regime, that we call the weighted integral method, was developed in [23] for flat space. The original $d=2$ integration variables in (7) are \vec{x} and \vec{y} . These variables are transformed to \vec{x} and $\vec{c} = \vec{y} - \vec{x}$. The Jacobian for this transformation equals 1. One interprets \vec{c} as a timelike future-pointing ‘defining vector’ for the causal interval from x to y in M . The variables \vec{x} then represent the position of the past endpoint of the interval. The point is that in the embedded regime the integrand does not depend on \vec{x} because the volume of the interval between x and y is a function of \vec{c} only and so the integral over \vec{x} can be done first, resulting in a factor we call the ‘volume of realisation’ $a(\vec{c})$. This is the volume in which the point x can be such that the defining vector \vec{c} starting at x fits within the manifold.

To find $a(\vec{c})$, we clone and displace the manifold by the defining vector. The volume of realisation equals the volume of the intersection of the two isometric shapes. This can be seen in figure 2 for a simple example, but will be true for any manifold in any dimension. Sometimes $a(\vec{c})$ is easy to calculate and then the remaining integration is performed over all future-pointing timelike defining vectors that can fit within the manifold. Following this method, the integral (7) becomes

$$X_\rho = \int_{c \in M} d^d c a(\vec{c}) e^{-\rho V_c}. \tag{14}$$

V_c is the volume of the causal interval defined by the vector \vec{c} . Note: we will sometimes use the notation $\vec{c} = (\Delta t, \Delta x_1, \dots, \Delta x_{d-1})$.

This method only works if the volume of the causal interval between \vec{x} and \vec{y} depends only on $\vec{c} = \vec{y} - \vec{x}$. This is true in the embedded regime and for globally hyperbolic manifolds—which are causally convex and so the two regimes coincide—but not for non-causally convex manifolds in the isolated regime. In the latter case, the causal interval will no longer be a complete diamond for intervals too close to a timelike boundary. We also cannot use this method in curved spacetime because defining vectors do not exist.

We can also use the weighted integral method to calculate the bi-action contributions. If we have two regions of the manifold X and Y , in order to find $\langle S_\rho^{(d)}(M; X, Y) \rangle$, we clone region Y and displace it by the defining vector \vec{c} . The volume of realisation for this defining vector equals the volume of the intersection of the displaced region Y and original region X . Then, defining vectors that can start in region Y and end in region X are integrated over.

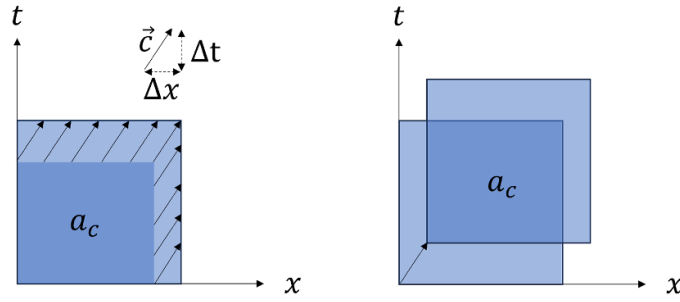


Figure 2. A $d = 2$ example, showing how by cloning the manifold and displacing it by the defining vector $\vec{c} = (\Delta t, \Delta x)$, the volume of realisation can be found from the overlapping area. The dark blue region on the left has an identical area to the overlapping area on the right.

2.7. Smearing to tame the fluctuations

The fluctuations of the random action around its expected value increase as ρ increases which makes it extremely challenging to discover the expected value in the $\rho \rightarrow \infty$ limit by performing simulations. In order to obtain useful results from simulations, it is useful to dampen these fluctuations by using a smeared form of the action, which introduces an intermediate length scale $l_k \geq l$. This smearing scale is parametrised by $\epsilon \leq 1$ which is defined as

$$\epsilon = \left(\frac{l}{l_k}\right)^d = \frac{K}{\rho}, \quad \text{where } K = \frac{1}{l_k^d}. \quad (15)$$

The smeared form of the action is based on the smearing of the causal set D'Alembertian introduced by Sorkin to dampen its fluctuations [27]. The smeared action is given by [7, 8]:

$$\frac{1}{\hbar} S_\epsilon^{(d)}(\mathcal{C}) = -\alpha_d \left(\frac{l}{l_p}\right)^{d-2} \left(\epsilon^{2/d} N + \frac{\beta_d}{\alpha_d} \epsilon^{(d+2)/d} \sum_{x \in \mathcal{C}} \sum_{y \prec x} f_d(n(x, y), \epsilon) \right) \quad (16)$$

where $n(x, y) = |[y, x]|$. Now the sum is over all pairs of related elements $y \prec x$ and

$$f_d(n, \epsilon) = (1 - \epsilon)^n \sum_{i=1}^{n_d} C_i^{(d)} \binom{n}{i-1} \left(\frac{\epsilon}{1 - \epsilon}\right)^{i-1}. \quad (17)$$

When $\epsilon = 1$, the smeared action equals the BDG action. The explicit forms of equation (16) for $d = 2, 3, 4$ that we used in the simulations are given in appendix A.

By Poisson sprinkling a manifold at density ρ and evaluating $S_\epsilon^{(d)}(\mathcal{C})$ for a given ϵ , $S_\epsilon^{(d)}(\mathcal{C})$ becomes the random variable $S_{\rho, K}^{(d)}(M)$. In the limit of infinite ρ , with K fixed, the mean of $S_{\rho, K}^{(d)}(M)$ equals the mean of the random BDG action with ρ replaced by K :

$$\lim_{\rho \rightarrow \infty} \frac{1}{\hbar} \langle S_{\rho, K}^{(d)}(M) \rangle = \frac{1}{\hbar} \langle S_K^{(d)}(M) \rangle. \quad (18)$$

Now the fluctuations of $\mathbf{S}_{\rho,K}^{(d)}(M)$ around its expected value die away as $\rho \rightarrow \infty$ (as $\epsilon \rightarrow 0$) so it is more suitable for simulations⁹. This advantage is gained however at the expense of needing to know the form of finite ρ corrections to the conjectures as we explain.

We expect that the mean of the original unsmeared random action at large, finite ρ will be an expansion like

$$\frac{1}{\hbar} \langle \mathbf{S}_{\rho}^{(d)}(M) \rangle = \frac{1}{l_p^{d-2}} (c_1 \rho^{\lambda_1} + c_2 \rho^{\lambda_2} + \dots + c_{n-1} \log \rho + c_n) \quad (19)$$

up to terms that are exponentially small for large ρ . The c_i are bulk and boundary-geometric quantities of the manifold times dimensionless constants and the powers λ_i of ρ ensure dimensional consistency. There may be other terms such as other log terms. This is a conjecture that includes both original conjectures (12) and (10) and that includes subleading terms in the expansion in ρ for large ρ .

The mean of the random smeared action will be dependent on the new scale K as well as on ρ . Equations (18) and (19) imply that in the limit of infinite ρ , with K fixed, the conjecture is

$$\lim_{\rho \rightarrow \infty} \frac{1}{\hbar} \langle \mathbf{S}_{\rho,K}^{(d)}(M) \rangle = \frac{1}{l_p^{d-2}} (c_1 K^{\lambda_1} + c_2 K^{\lambda_2} + \dots + c_{n-1} \log K + c_n) \quad (20)$$

where the geometric quantities and exponents are the same as before and the only difference is that K has replaced ρ . For example, in the case of a manifold with timelike boundaries, conjecture 1' becomes

$$\lim_{\rho \rightarrow \infty} \frac{1}{\hbar} \langle \mathbf{S}_{\rho,K}^{(d)}(M) \rangle = \frac{1}{\hbar} \langle \mathbf{S}_K^{(d)}(M) \rangle = \frac{1}{l_p^{d-2}} a_d^{\text{emb/iso}} \text{Vol}_{d-1}(T) K^{\frac{1}{d}} + \text{subleading}. \quad (21)$$

When ρ is finite, we expect there to be corrections to this expression that depend on both K and ρ , $E_{K,\rho}$:

$$\frac{1}{\hbar} \langle \mathbf{S}_{\rho,K}^{(d)}(M) \rangle = \frac{1}{\hbar} \langle \mathbf{S}_K^{(d)}(M) \rangle + E_{K,\rho}. \quad (22)$$

In all of the simulations that follow, we fixed $\epsilon = 0.1$, i.e. $K = \rho/10$, and we varied the sprinkling density ρ . Increasing ρ therefore increases K . This value of ϵ was chosen as a compromise between reducing the fluctuations about the expected value (achieved by a smaller value of epsilon) and reducing the computation time (which increases as rho increases, so a smaller value of epsilon will result in longer computation times for a given range of K values).

3. Timelike boundaries in 1+1 dimensions

All the examples in this section are in the embedded regime.

3.1. Triangle in 1+1

As our first example of a spacetime region with timelike boundaries, we considered the triangle shown in the far left of figure 3. This has two null and one timelike edge. Coordinates (t, x) have origin at the bottom corner of the triangle and we use null coordinates $u = \frac{1}{\sqrt{2}}(t - x)$ and

⁹ It is an open question whether the smeared version of the action should be used in the path integral instead of the BDG action. We will not take a position on this here, but will use the smeared action to do simulations to obtain evidence for the conjectures.

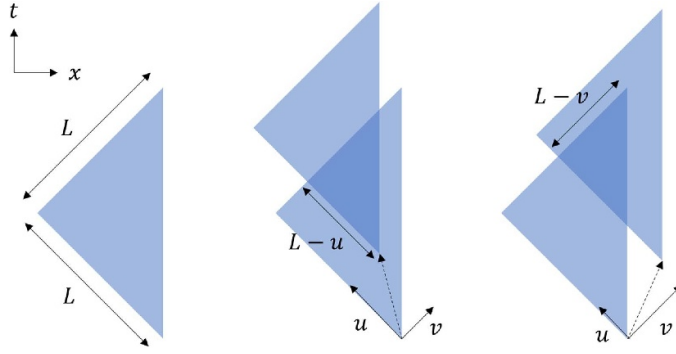


Figure 3. Triangular manifold (left) and its area of realisation (= area of overlapping region) with $u > v$ (middle) and $v > u$ (right).

$v = \frac{1}{\sqrt{2}}(t + x)$. Using the weighted integral method, we consider the vector (u, v) (working in null coordinates) that defines an interval that can fit within this region. To find the volume of realisation, the situations $u > v$ and $v > u$ must be considered separately. This is shown in figure 3

We find,

$$\begin{aligned} X_\rho &= \int_0^L du \int_0^u dv \frac{1}{2} (L - u)^2 e^{-\rho uv} + \int_0^L dv \int_0^v du \frac{1}{2} (L - v)^2 e^{-\rho uv} \\ &= 2 \int_0^L du \int_0^u dv \frac{1}{2} (L - u)^2 e^{-\rho uv} \end{aligned} \quad (23)$$

and (8) gives

$$\begin{aligned} \frac{1}{\hbar} \langle S_\rho(M) \rangle &= 2\rho V - 4\rho^2 \hat{O}_2 X_\rho \\ &= \frac{1}{2} \sqrt{\pi} L \sqrt{\rho} \text{Erf}(L\sqrt{\rho}) \end{aligned} \quad (24)$$

where Erf is the error function. This expression does not have the +1 contribution which we might have expected from the joint (left corner). This is further investigated in section 3.2 and appendix B. The length of the timelike boundary for this manifold is $T = \sqrt{2}L$ and, we have in the limit,

$$\lim_{\rho \rightarrow \infty} \frac{1}{\hbar} \langle S_\rho(M) \rangle \sim \frac{1}{2} \sqrt{\frac{\pi}{2}} T \sqrt{\rho} \quad (25)$$

which agrees with conjecture 2 and the value of $a_2^{\text{emb}} = \frac{1}{2} \sqrt{\frac{\pi}{2}}$ found in [23].

3.2. 1+1 Infinite t

The next shape for which we compute the action is a slab, which is finite in the x direction and infinite in the t direction. This manifold is depicted in figure 4.

The volume of realisation is

$$a(\vec{c}) = (L - \Delta x) \left(\int_{-\infty}^{\infty} dt \right) \quad (26)$$

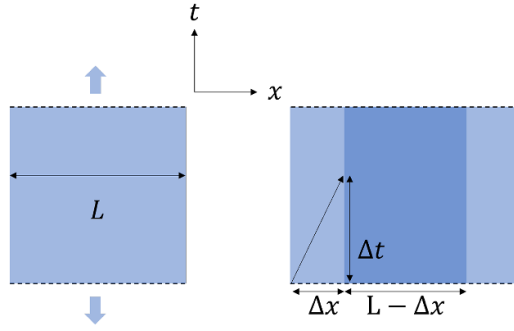


Figure 4. Left: a spacetime region with infinite timelike boundaries. Right: cloning the region to obtain the volume of realisation, shown in dark blue.

as the length in the t direction of this volume is infinite. For the vector to define an interval, $|\Delta x| < \Delta t$. However, the defining vector will only fit within the manifold if $|\Delta x| < L$. The integral is a sum of 2 integrals for $\Delta t < L$ and $\Delta t > L$:

$$X_\rho = 2 \int_{-\infty}^{\infty} dt \left(\int_0^L d\Delta t \int_0^{\Delta t} d\Delta x + \int_L^{\infty} d\Delta t \int_0^L d\Delta x \right) (L - \Delta x) e^{-\frac{1}{2}\rho(\Delta t^2 - \Delta x^2)}. \quad (27)$$

The factor of 2 is due to symmetry when including the contribution from $\Delta x < 0$. The action is then given by

$$\frac{1}{\hbar} \langle S_\rho(M) \rangle = 2\rho V - 4\rho^2 \hat{\mathcal{O}}_2 X_\rho = \int_{-\infty}^{\infty} dt \sqrt{\frac{\pi}{2}} \sqrt{\rho} + \mathcal{O}\left(\frac{1}{\rho}\right). \quad (28)$$

For this manifold, the volume of the timelike boundary is $T = 2 \left(\int_{-\infty}^{\infty} dt \right)$ since there are 2 boundaries. We therefore find

$$\lim_{\rho \rightarrow \infty} \frac{1}{\hbar} \langle S_\rho(M) \rangle \sim \frac{1}{2} \sqrt{\frac{\pi}{2}} T \sqrt{\rho}, \quad (29)$$

consistent with the conjecture and $a_2^{\text{emb}} = \frac{1}{2} \sqrt{\frac{\pi}{2}}$.

Moreover, from equation (28), we see that the mean of the action does not contain any constant terms. This is an interesting result, suggesting the boundary itself does not give any constant terms, and only contributes the conjectured term in the infinite density limit. Therefore, we might suspect the missing +1 term from the causal triangle in section 3.1 was not cancelled out by the lower ordered timelike boundary terms, but by something else. A good candidate is the top and bottom corners of the triangle (the intersection between a null boundary and a timelike boundary), which each contribute $-\frac{1}{2}$ to the action. This is of minor importance however, since the action is always dominated by the term from the timelike boundary. A contribution from the intersection between a general timelike and a null/spacelike boundary is conjectured in appendix C.

4. d -dimensional infinite slab in the embedded regime

4.1. Set-up

Assuming universality of the constant a_d^{emb} , we choose a convenient manifold with a time-like boundary to calculate a_d^{emb} : the d dimensional ‘infinite slab’. This manifold is given by $t \in [0, T]$, $x_1 \in [0, L]$ with $T \leq L$, and all other coordinates are unbounded $-\infty < x_i < \infty$, $i = 2, 3 \dots d-1$. For such a slab in d dimensions, the conjecture (12) becomes:

$$\lim_{\rho \rightarrow \infty} l_p^{d-2} \frac{1}{\hbar} \langle S_\rho^{(d)}(M) \rangle \rho^{-\frac{1}{d}} = a_d^{\text{emb}} \int_{-\infty}^{\infty} dx_2 \dots \int_{-\infty}^{\infty} dx_{d-1} 2T. \quad (30)$$

We again use the weighted integral method. The defining vector has components $\vec{c} = (\Delta t, \Delta x_1, \Delta x_2, \dots, \Delta x_{d-1})$. We find

$$\begin{aligned} X_\rho(d) = & \int_0^T d\Delta t \int_{-\Delta t}^{\Delta t} d\Delta x_1 \int_{-\sqrt{\Delta t^2 - \Delta x_1^2}}^{\sqrt{\Delta t^2 - \Delta x_1^2}} d\Delta x_2 \dots \int_{-\sqrt{\Delta t^2 - \Delta x_1^2 - \Delta x_2^2}}^{\sqrt{\Delta t^2 - \Delta x_1^2 - \Delta x_2^2}} d\Delta x_{d-1} \\ & \times \int_{-\infty}^{\infty} dx_2 \dots \int_{-\infty}^{\infty} dx_{d-1} (L - |\Delta x_1|) (T - \Delta t) e^{-\rho V_c(d)} \end{aligned} \quad (31)$$

where the limits of the integral in the first line ensure that the defining vector is timelike and future pointing.

The volume of the interval (causal diamond) $V_c(d)$ is a function of the proper height of the interval i.e. the proper length of the defining vector $c = |\vec{c}|$:

$$V_c(d) = \frac{\tau}{d} V_{\text{ball}}(d-1) = \frac{\tau \pi^{(d-1)/2} \left(\frac{c}{2}\right)^{d-1}}{d \Gamma((d+1)/2)} \quad (32)$$

where $V_{\text{ball}}(d-1)$ is the volume of the $(d-1)$ dimensional ball with radius $c/2$.

For the rest of this section, we will suppress mention of the integrals $\int_{-\infty}^{\infty} dx_2 \dots \int_{-\infty}^{\infty} dx_{d-1}$ which are implied.

We switch to radial spherical polar variables for the spatial components of \vec{c} including

$$\Delta r = \sqrt{\Delta x_1^2 + \Delta x_2^2 \dots + \Delta x_{d-1}^2}, \quad (33)$$

and define null radial variables

$$v = \frac{1}{\sqrt{2}} (\Delta t + \Delta r), u = \frac{1}{\sqrt{2}} (\Delta t - \Delta r). \quad (34)$$

We find

$$\begin{aligned} X_\rho(d) = & - \int_0^{\frac{T}{\sqrt{2}}} du \int_u^{\sqrt{2}T-u} dv e^{-\rho V_c(d)} \\ & \times \frac{(2\pi)^{\frac{d}{2}-2} (v-u)^{d-2} \left(\sqrt{2}(u+v) - 2T\right) \left(2\pi L \Gamma\left(\frac{d}{2}\right) + \sqrt{2\pi} \Gamma\left(\frac{d-1}{2}\right) (u-v)\right)}{\Gamma(d-1)} \end{aligned} \quad (35)$$

where

$$V_c(d) = \frac{2^{1-\frac{d}{2}} \pi^{\frac{d-1}{2}} (uv)^{d/2}}{d \Gamma\left(\frac{d+1}{2}\right)}. \quad (36)$$

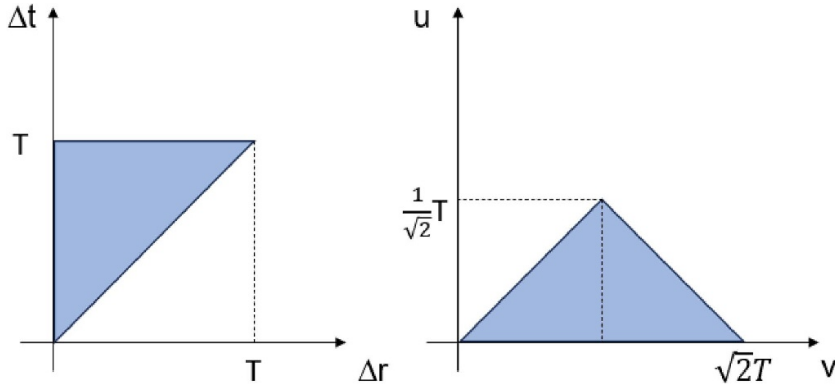


Figure 5. Left: the area of integration in $\Delta t, \Delta r$ space. Right: the area of integration in u, v space.

The range of the u, v integration is within the area $\int_0^T d\Delta t \int_0^{\Delta t} dr$, shown in figure 5 both in $\Delta t, r$ and u, v coordinates. We rename $X_\rho = X_\rho^{(1)}$ for reasons that will be clear in the next section. We are not able to evaluate this integral analytically.

4.2. Extending the triangle

For the conjecture, we are interested in the limit of large ρ . Observing the exponent of equation (35) (i.e. $V_c(d)$ from equation (36)), we note the integrand is exponentially suppressed when both u and v are bounded away from zero. Therefore, the non-exponentially suppressed contribution comes from close to $u = 0$ or $v = 0$. This idea inspires an approximation of $X_\rho = X_\rho^{(1)}$ in (35) by extending the range of integration to the full triangle shown in figure 6. This extended range is the union of region 1, the original range, and an extra region 2. In appendix D, we show that the integral over region 2 alone tends to zero as $\rho \rightarrow \infty$, using both numerical and analytical arguments. Thus, extending the range of integration does not change the leading order behaviour of $X_\rho = X_\rho^{(1)}$ as $\rho \rightarrow \infty$. Therefore the new terms that arise due to this approximation are subleading and vanish in the continuum limit.

We have

$$X_\rho^{\text{extended}}(d) = X_\rho^{(1)}(d) + X_\rho^{(2)}(d) = - \int_0^{\sqrt{2}T} du \int_u^{\sqrt{2}T} dv e^{-\rho V_c(d)} \times \frac{(2\pi)^{\frac{d}{2}-2} (v-u)^{d-2} \left(\sqrt{2}(u+v) - 2T \right) \left(2\pi L\Gamma\left(\frac{d}{2}\right) + \sqrt{2\pi}\Gamma\left(\frac{d-1}{2}\right)(u-v) \right)}{\Gamma(d-1)}, \quad (37)$$

where the superscript refers to the region in which the integral is performed i.e. $X_\rho^{(1)}$ is the integral evaluated in region 1, and $X_\rho^{(2)}$ in region 2. The integral with the extended range can be performed analytically in any chosen dimension and then using operator \hat{O}_d , the leading order of the mean action can be found.

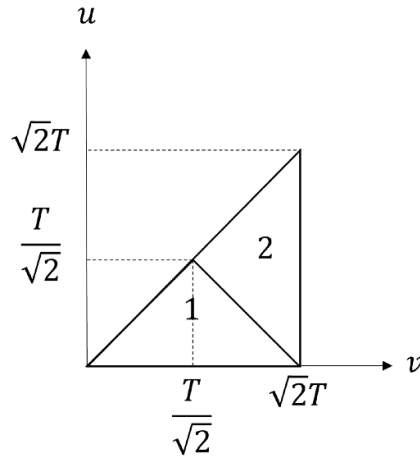


Figure 6. Extending the shape in figure 5(right).

4.3. Results

The mean of the action calculated as described above is consistent with conjecture (30) in every dimension up to and including $d = 17$ with coefficients a_d^{emb} given by

$$a_d^{\text{emb}} = \begin{cases} \frac{2^{-\frac{1}{d}} \pi^{-\frac{1}{2d}} (\Gamma(\frac{d+1}{2})d)^{-\frac{1}{d}}}{\Gamma(\frac{1}{2} + \frac{1}{d})}, & \text{odd } d \\ \frac{2^{-\frac{1}{d}-1} \pi^{-\frac{1}{2d}+1} (\Gamma(\frac{d+1}{2})d)^{-\frac{1}{d}}}{\Gamma(\frac{1}{2} + \frac{1}{d})}, & \text{even } d. \end{cases} \quad (38)$$

where $\Gamma(x)$ is the Gamma function. We conjecture that these formulae hold for all d .

For $d = 3$ specifically, if we integrate over the extended triangle, and then subtract the leading order contribution from region 2, then we find that the mean of the action has the form of

$$\frac{1}{\hbar} \langle S_\rho^{(d=3)}(M) \rangle = \frac{1}{l_p} \left(c_1 \rho^{1/3} + c_2 \rho^{-1/3} + \dots \right), \quad (39)$$

for finite ρ in the large ρ expansion, where c_1 and c_2 are constants. In what follows we will assume this form of finite ρ correction when we assess and fit computational results for other $d = 3$ manifolds, as the corrections to the leading term will not be negligible.

5. Simulations of timelike boundaries

5.1. Simulation of $d = 3$ ball in embedded regime

In order to test the conjecture with a manifold with curved timelike boundaries, using (38), we sprinkled a region of $d = 3$ Minkowski space that is a ball of Euclidean coordinate radius R in the embedded regime, see figure 7.

The area of the timelike boundary is $V = \pi^2 R^2 / \sqrt{2}$ and the conjecture for the action for this manifold is:

$$\lim_{\rho \rightarrow \infty} l_p \frac{1}{\hbar} \langle S_\rho^{(3)}(M) \rangle \rho^{-\frac{1}{3}} = \frac{\pi^2}{\sqrt{2}} R^2 a_3^{\text{emb}}. \quad (40)$$

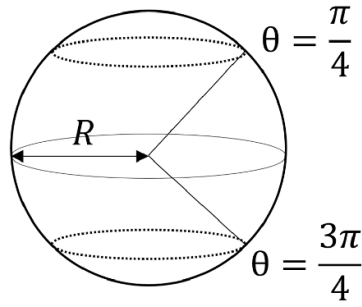


Figure 7. The timelike boundary is the surface between the 2 dotted lines.

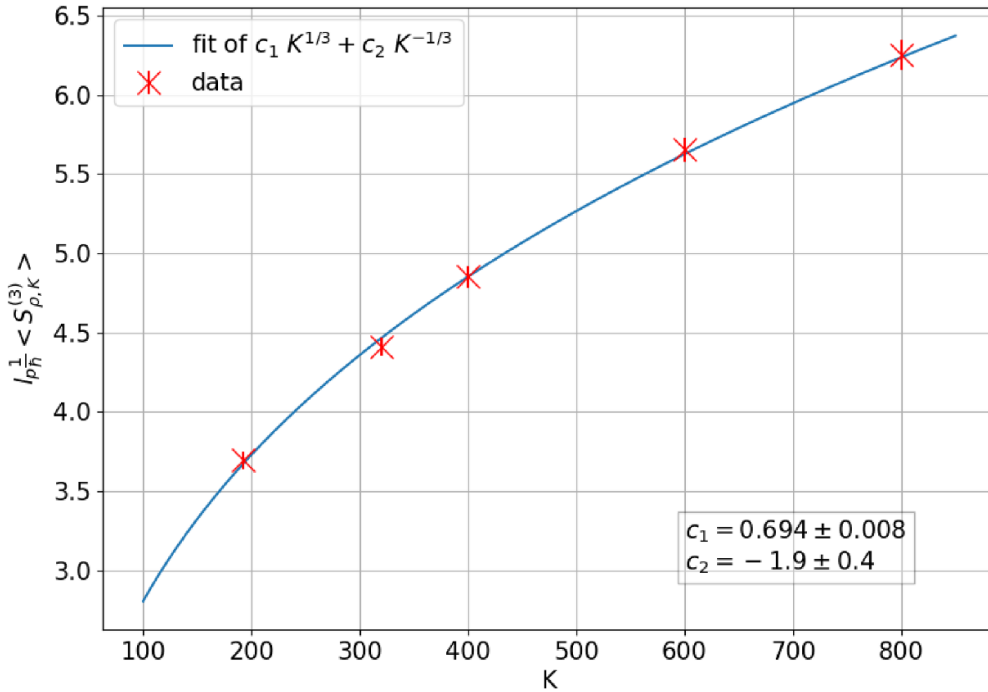


Figure 8. The sample mean of the action of the sphere against K , with a curve fitted to the data (blue). The sphere has radius 0.5.

5.1.1. Results. The random smeared action was sampled by sprinkling, for $R=0.5$. As described in section 2.7, the conjecture implies for fixed K that (21)

$$\lim_{\rho \rightarrow \infty} l_p \frac{1}{\hbar} \langle S_{\rho,K}^{(3)}(M) \rangle = \frac{\pi^2}{4\sqrt{2}} a_3^{\text{emb}} K^{\frac{1}{3}} + c_2 K^{-\frac{1}{3}} + o\left(K^{-\frac{1}{3}}\right) \tag{41}$$

where we have assumed the first correction has the same form as in the calculation for the $d=3$ infinite slab (39).

In the simulations $\epsilon=0.1$ is fixed so that $K = \rho/10$ and the sprinkling density ρ was varied. For each ρ , the sample mean of the action over 100 sprinklings was calculated, the results are shown in figure 8 and the data are fitted by a function with the expected form $c_1 K^{1/3} +$

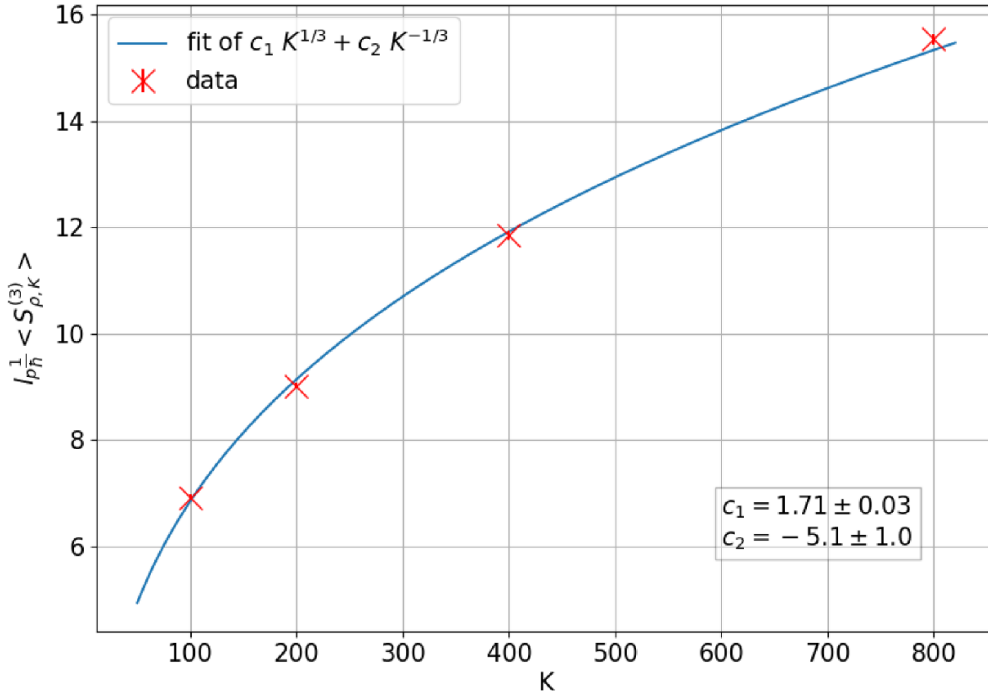


Figure 9. The sample mean of the action of the cube against K , with a curve fitted to the data (blue). The cube has side length 1.

$c_2 K^{-1/3}$. This gives best fit values $c_1 = 0.694 \pm 0.008$ and $c_2 = -1.9 \pm 0.4$. This gives $a_3^{\text{emb}} = 0.398 \pm 0.005$ which is consistent with the analytic value from the $d = 3$ infinite slab $a_3^{\text{emb}} = \frac{\sqrt[3]{\frac{3}{\pi}} \Gamma(\frac{1}{3})}{3\pi^{2/3} \Gamma(\frac{5}{3})} \simeq 0.403$.

The data are consistent with the conjecture, however it is worth keeping in mind, here and for the other simulations, that the behaviour explored is for fixed $\epsilon = K/\rho$ and there should be unknown ϵ dependent corrections.

5.2. Simulation of $d = 3$ cube, isolated

The isolated regime is the physically relevant one when considering the sprinkled causal sets as contributing to the causal set Sum Over Histories as individual discrete spacetimes in their own right. We chose to sample the random smeared action in the isolated regime for a unit cube in $d = 3$. The volume of the timelike boundary equals 4.

For each ρ , the sample mean of the action over 200 sprinklings is shown in figure 9 and the data are fitted by a function with the same form as before $c_1 K^{1/3} + c_2 K^{-1/3}$. This gives best fit values $c_1 = 1.71 \pm 0.03$ and $c_2 = -5.1 \pm 1.0$ which gives $a_3^{\text{iso}} = 0.428 \pm 0.008$. In this case we do not have an analytic calculation of a_3^{iso} to compare to.

We conclude that the $d = 3$ cube in the isolated regime is consistent with the same conjecture as the embedded regime but with a different coefficient. Note that $a_3^{\text{iso}} > a_3^{\text{emb}}$, as was also the case for $d = 2$ case. This makes sense because V_{xy} is smaller in the isolated regime, so the exponent in the integral is less negative, resulting in a larger action.

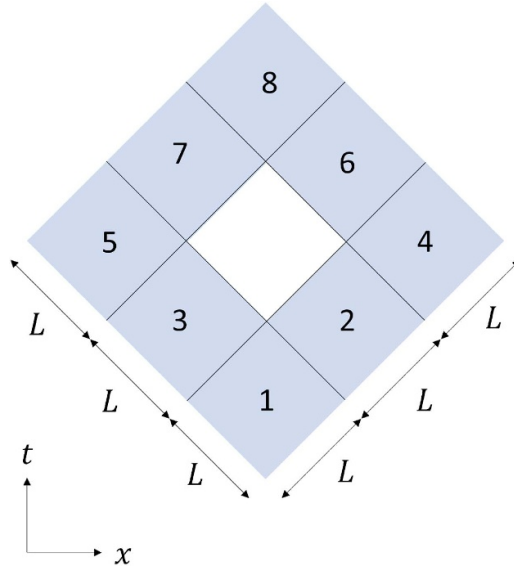


Figure 10. The annulus in Cartesian coordinates. The hole is centred and is a ninth of the total area of the diamond.

6. Holes

We turn to a different class of non-globally hyperbolic spacetimes: spacetimes with holes.

6.1. Isolated annulus

The null annulus—a causal diamond with a diamond removed from the centre—is the simplest example of a hole for $d = 2$. An example is shown in figure 10.

In the embedded regime the continuum limit of the mean random action of a null annulus can be calculated using the ‘topological calculus’ of [26] and equals 4 no matter the size of the diamond, the size of the hole or where the hole is [23].

In the isolated regime, the calculation can still be done analytically by partitioning the manifold into the regions shown in figure 10 and using the bilocal action formula:

$$\langle \mathcal{S}_{\text{annulus}} \rangle = \sum_{i=1}^8 \langle \mathcal{S}_i \rangle + \sum_{\substack{i,j=1 \\ j < i}}^8 \langle \mathcal{S}_{i,j} \rangle. \quad (42)$$

$\langle \mathcal{S}_i \rangle$ is the action of a causal diamond and is the same for all 8. From symmetry, many of the $\langle \mathcal{S}_{i,j} \rangle$ are identical. We can separate these into 5 different categories and within each category, the terms are equal:

- $(i,j) = (2,1), (4,2), (6,4), (8,6), (3,1), (5,3), (7,5)$ and $(8,7)$.
- $(i,j) = (4,1), (8,4), (5,1)$ and $(8,5)$.
- $(i,j) = (6,1), (8,2), (7,1)$ and $(8,3)$
- $(i,j) = (6,2), (7,3)$
- $(i,j) = (8,1)$.

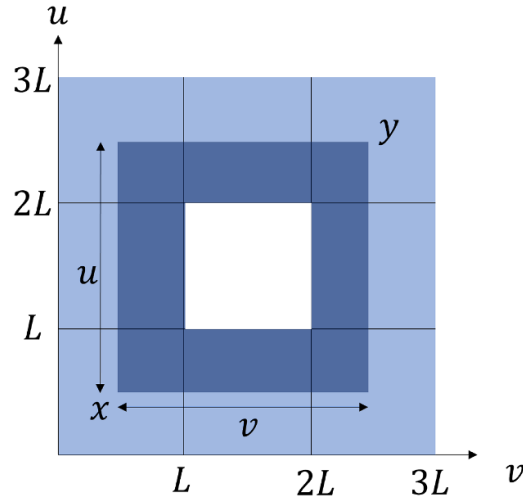


Figure 11. For an interval starting at any point x in region 1 and ending at any point y in region 8, the volume of the interval (shown in dark blue) will always be uv minus the area of the hole (white).

Therefore (42) can be simplified to:

$$\lim_{\rho \rightarrow \infty} \frac{1}{\hbar} \langle \mathcal{S}_{\text{annulus}} \rangle = \lim_{\rho \rightarrow \infty} \frac{1}{\hbar} (8 \langle \mathcal{S}_{\text{diamond}} \rangle + 8 \langle \mathcal{S}_{2,1} \rangle + 4 \langle \mathcal{S}_{4,1} \rangle + 4 \langle \mathcal{S}_{6,1} \rangle + 2 \langle \mathcal{S}_{6,2} \rangle + \langle \mathcal{S}_{8,1} \rangle). \quad (43)$$

From [26] we have¹⁰

$$\begin{aligned} \lim_{\rho \rightarrow \infty} \frac{1}{\hbar} \langle \mathcal{S}_{\text{diamond}} \rangle &= 2, & \lim_{\rho \rightarrow \infty} \frac{1}{\hbar} \langle \mathcal{S}_{2,1} \rangle &= -2, & \lim_{\rho \rightarrow \infty} \frac{1}{\hbar} \langle \mathcal{S}_{4,1} \rangle &= 0, \\ \lim_{\rho \rightarrow \infty} \frac{1}{\hbar} \langle \mathcal{S}_{6,2} \rangle &= \lim_{\rho \rightarrow \infty} 2 \left(\gamma - 1 + \ln L^2 \rho + \mathcal{O}\left(\frac{1}{\rho}\right) \right) \sim 2 \ln \rho. \end{aligned} \quad (44)$$

In the last expression, the $\ln \rho$ term dominates over the constant terms and the limit is divergent. It remains to compute $\langle \mathcal{S}_{8,1} \rangle$ and $\langle \mathcal{S}_{6,1} \rangle$.

6.1.1. Region 1 to 8. We use the weighted integral method. From figure 11 we see the interval defined by the vector (u, v) will always have an area of $uv - L^2$, where $u = u_y - u_x$ and $v = v_y - v_x$.

There are 4 separate cases for the volume of realisation shown in figure 12 and X_ρ equals

$$\begin{aligned} X_\rho &= \int_L^{2L} du \left[\int_L^{2L} dv (u-L)(v-L) e^{-\rho(uv-L^2)} + \int_{2L}^{3L} dv (u-L)(3L-v) e^{-\rho(uv-L^2)} \right] \\ &+ \int_{2L}^{3L} du \left[\int_L^{2L} dv (3L-u)(v-L) e^{-\rho(uv-L^2)} + \int_{2L}^{3L} dv (3L-u)(3L-v) e^{-\rho(uv-L^2)} \right]. \end{aligned} \quad (45)$$

¹⁰ Note the action we use here has an additional factor of 2 compared to the action in [26].

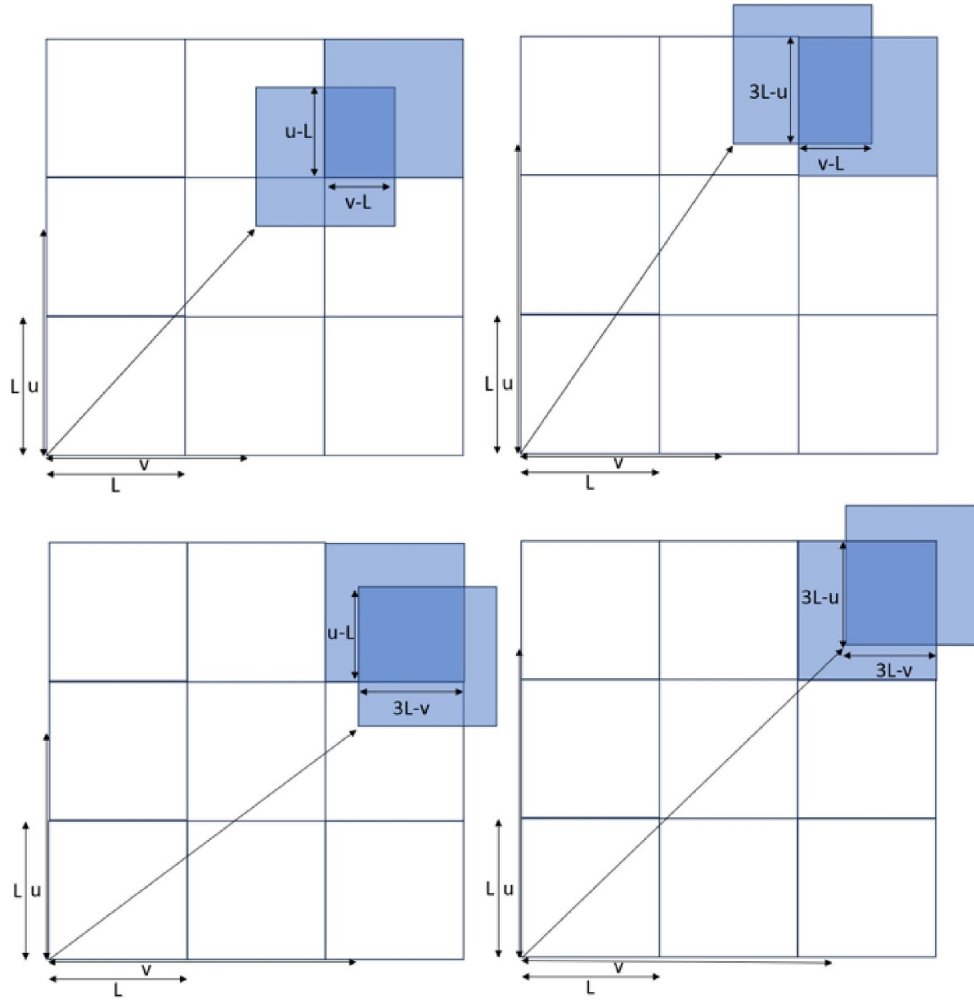


Figure 12. The 4 possible volumes of realisation for different ranges of u and v .

All the integrals are exponentially small as $\rho \rightarrow \infty$ and

$$\lim_{\rho \rightarrow \infty} \frac{1}{\hbar} \langle \mathcal{S}_{8,1} \rangle = \lim_{\rho \rightarrow \infty} \left(-4\rho^2 \hat{\mathcal{O}}_2 X_\rho \right) = 0. \quad (46)$$

6.1.2. *Region 1 to 6.* We have as shown in figure 13

$$X_\rho = \int_0^L dv_x \int_0^L du_x \int_L^{2L} du_y \int_{2L}^{3L} dv_y e^{-\rho((u_x - u_y)(v_x - v_y) - (2L - v_x)(u_y - L))}, \quad (47)$$

which gives

$$\lim_{\rho \rightarrow \infty} \frac{1}{\hbar} \langle \mathcal{S}_{6,1} \rangle = \lim_{\rho \rightarrow \infty} \left(-4\rho^2 \hat{\mathcal{O}}_2 X_\rho \right) = \ln 4. \quad (48)$$

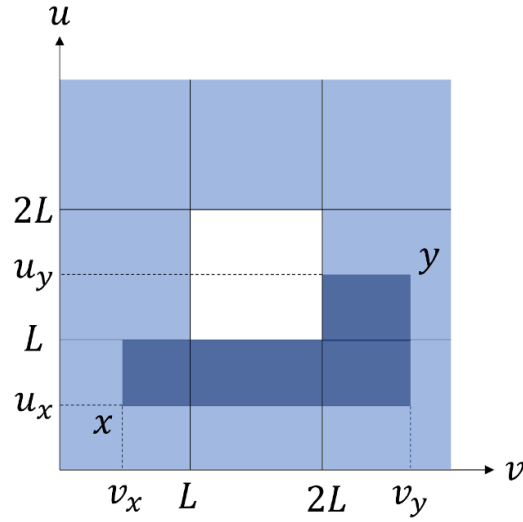


Figure 13. For an interval starting at any point x in region 1 and ending at any point y in region 6, the volume of the interval is shown in dark blue.

6.1.3. *Full result.* Combining these results, we obtain

$$\lim_{\rho \rightarrow \infty} \frac{1}{\hbar} \langle \mathcal{S}_{\text{annulus}} \rangle = \lim_{\rho \rightarrow \infty} 4 (\ln L^2 \rho + \ln 4 + \gamma - 1) \quad (49)$$

which diverges logarithmically.

6.1.4. *Simulations.* The results of our simulations for this manifold and one variant are shown in figure 14. The causal diamond has side length 1 and the size of the hole was varied. The case of the previous section corresponds to $L = \frac{1}{3}$. The equation of the blue line in figure 14 is given by:

$$4 \left(\ln \frac{K}{9} + \ln 4 + \gamma - 1 \right) \quad (50)$$

and the data is consistent with it.

We fit $c_1 \ln K + c_2$ to the data for the hole of length $\frac{3}{5}$ to find $c_1 = 3.95 \pm 0.07$ (and $c_2 = -3.1 \pm 0.3$). This suggests that the leading order term for any sized hole will be $4 \ln \rho$ which is consistent with the log term originating from $\langle \mathcal{S}_{6,2} \rangle$. This is therefore likely to be the dominant term for any sized hole. We conclude that for a null annulus, the mean action diverges logarithmically with the density of sprinkling, regardless of the size of the hole.

6.2. Spacelike holes

We investigate another type of hole, one which has only spacelike boundaries such as figure 15(a). We argue that the contribution of such a hole to the action will be logarithmically divergent, as for a null hole.

The argument is as follows. A causal curve involving points in region 9 can only begin in regions 1, 2, 3, or 9, and must end in region 9. Let us denote the union of these four regions $1 \cup 2 \cup 3 \cup 9$. The contribution of $1 \cup 2 \cup 3 \cup 9$ to the limiting mean action equals the contribution

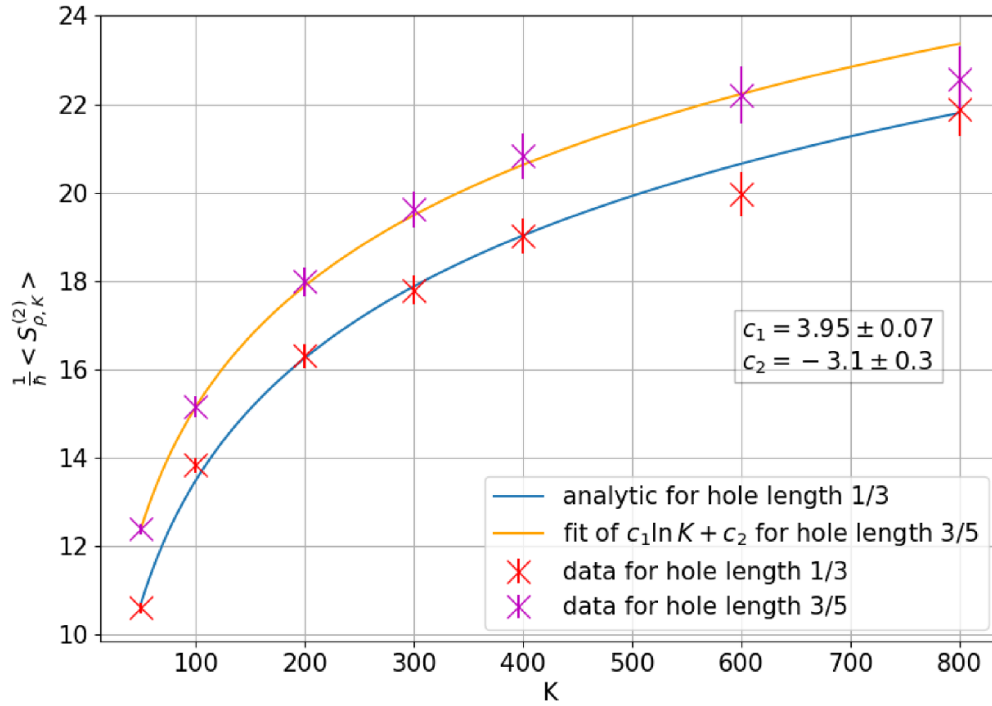


Figure 14. Sample mean action vs K for the null annulus with different sized holes.

of $1 \cup 2 \cup 3$ to the limiting mean action of the null annulus (without 9) because (i) $1 \cup 2 \cup 3 \cup 9$ is globally hyperbolic in itself, so its mean action equals the mean action of $1 \cup 2 \cup 3$ by conjecture (10), and (ii) the bilocal contribution to the action from $1 \cup 2 \cup 3 \cup 9$ is unchanged by deleting 9, since there are no causal curves between 9 and the complement of $1 \cup 2 \cup 3 \cup 9$. There's a similar argument for region 10. Therefore, the limiting mean action for the diamond with the spacelike hole equals that for the null annulus.

We performed a simulation for the diamond with $L' = 1$ and a spacelike hole as shown in figure 15(b). The joints of the hole have a small Lorentzian angle (to be defined in the next section), so this manifold and the null annulus are distinguishable at finite ρ .

The data is shown in figure 16, and is fitted to the function $c_1 \ln(L'^2 K) + c_2$. The best fit is for $c_1 = 4.03 \pm 0.17$, which is consistent with the argument given above, and $c_2 = -3.6 \pm 0.9$. The data from the null hole and spacelike hole have overlapping error bars, consistent with the argument above that adding/deleting regions 9 and 10 does not change the mean action. One could flatten the hole to just a deleted line segment and the mean action would be unchanged.

In the statement of conjecture 1 for globally hyperbolic spacetimes, the joint was defined as the co-dimension 2 intersection of the future boundary and the past boundary of the spacetime. In the non-globally hyperbolic spacetimes with spacelike holes that we have just considered, we can extend the definition of joint. For, a spacetime with a spacelike hole has a past boundary and a future boundary at the hole, where causal curves enter and leave the spacetime respectively, and these boundaries also intersect. We can distinguish between the two cases as follows. We define a joint to be a *convex joint* when there exists a future directed causal curve from the past boundary to the future boundary—the globally hyperbolic case—and otherwise the joint is a *concave joint*.

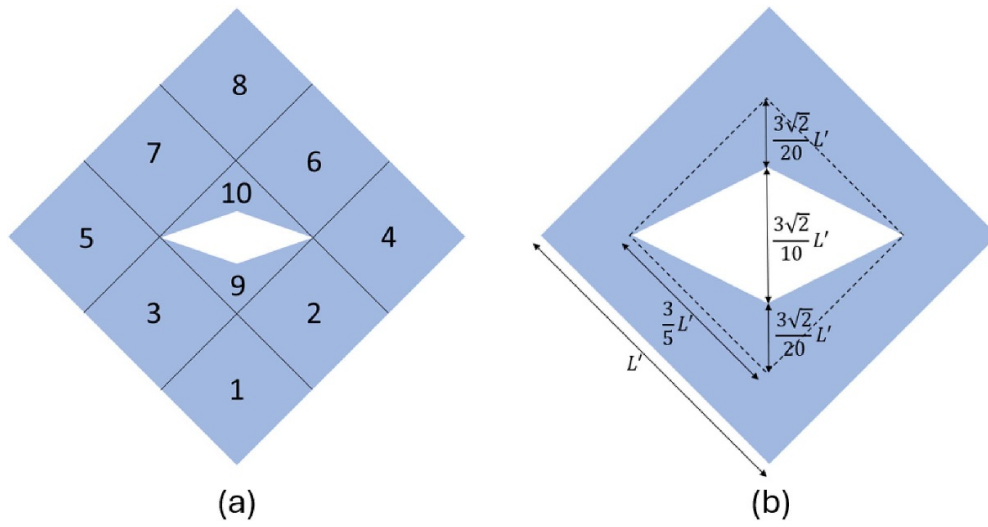


Figure 15. (a) A $d=2$ causal diamond with a spacelike hole. Note the new regions 9 and 10. (b) A $d=2$ causal diamond with side L' with a spacelike hole. The dimensions of the hole are labelled.

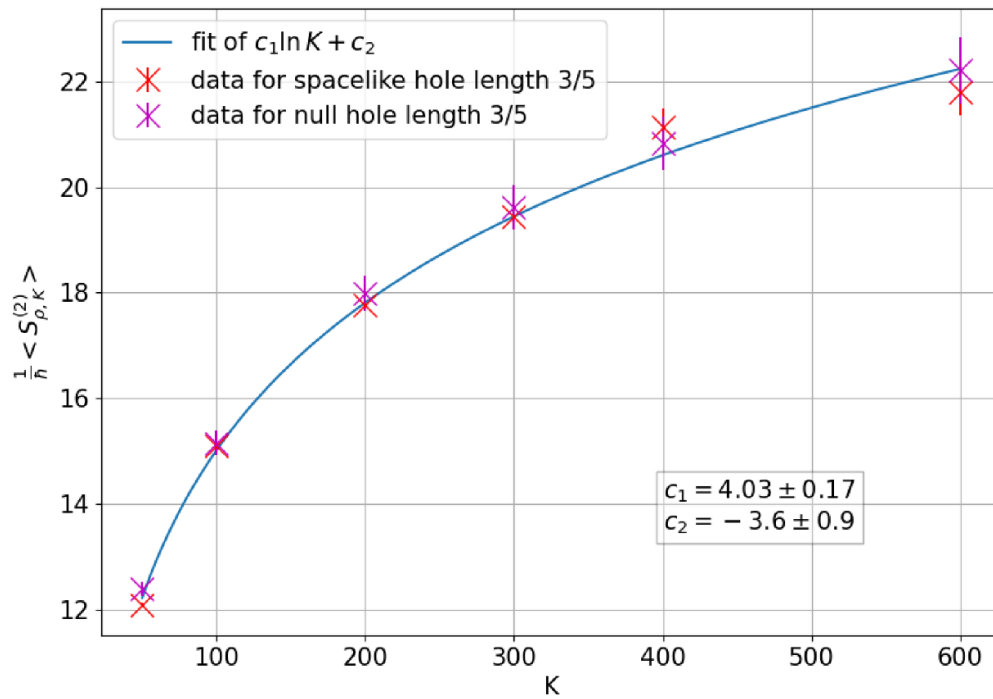


Figure 16. Sample mean and standard error of the action for the $L' = 1$ diamond with a spacelike and also with a null hole. The blue curve is fitted to the spacelike data (red).

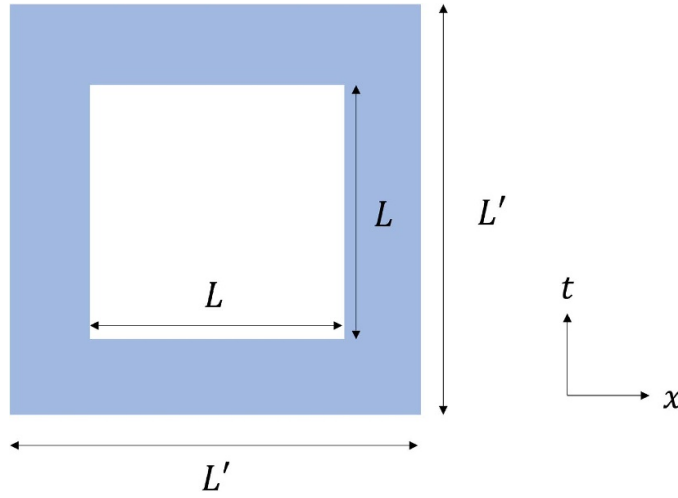


Figure 17. The square hole.

We propose a new conjecture for a concave joint, that its contribution to the mean action obeys:

$$\lim_{\rho \rightarrow \infty} \frac{1}{\hbar} \langle \mathbf{S}^{(d)} [\mathcal{M}] \rangle \sim \frac{1}{l_p^{d-2}} b_d \text{Vol}_{d-2}(J') \ln(\rho V) \quad (51)$$

where b_d is a dimensional coefficient, and J' is the concave joint. The contribution (51) is dimensionally correct and is proportional to the volume of the concave joint as one might expect. The results of sections 6.1 and 6.2 are evidence for the conjecture for $d = 2$ with $b_{d=2} = 2$. More evidence is needed, especially for more than 2 dimensions.

6.3. Timelike holes

A square with a square hole in its centre is an example of a manifold with a timelike hole (shown in figure 17). In [23], the mean action in the embedded regime was found to be consistent with the timelike boundary conjecture, i.e. the leading order term was of the form $2(L' + L)a_2^{\text{mb}}\rho^{\frac{1}{2}}$. L' is the side length of the square and L the side length of the hole, so $2(L' + L)$ is the length of the full timelike boundary. The same leading behaviour—with a different coefficient—is expected in the isolated regime, and we investigated this using simulations.

For square holes with lengths $L = \frac{3}{5}L'$ and $L = \frac{1}{5}L'$ (with $L' = 1$) the results are shown in figure 18.

We do not fit for a_2^{iso} but assume its value is $a_2^{\text{iso}} = 0.6959$ from [23]. The subleading $\ln \rho$ term in the fitting function is taken from the results for the null hole and we conjecture that it originates from the corners of the hole. Including this term is not enough, however, to give a good fit to the data and we also included a constant term.

The fitted coefficients of the log terms were $c_1 = 3.68 \pm 0.33$ for $L = \frac{3}{5}L'$ and $c_3 = 3.96 \pm 0.78$ for $L = \frac{1}{5}L'$. These two values are consistent, implying that the log contribution is the same regardless of the hole size, as was the case for the null hole. The fitted values of the constant term were $c_2 = -18.7 \pm 2.0$ for $L = \frac{3}{5}L'$ and $c_4 = -15.6 \pm 4.5$ for $L = \frac{1}{5}L'$.

The main conjecture is the behaviour of the leading order term, $a_2^{\text{iso}} \text{Vol}(\text{T})K^{\frac{1}{2}}$, consistent with the timelike boundary conjecture. We can say that the data are consistent with this but

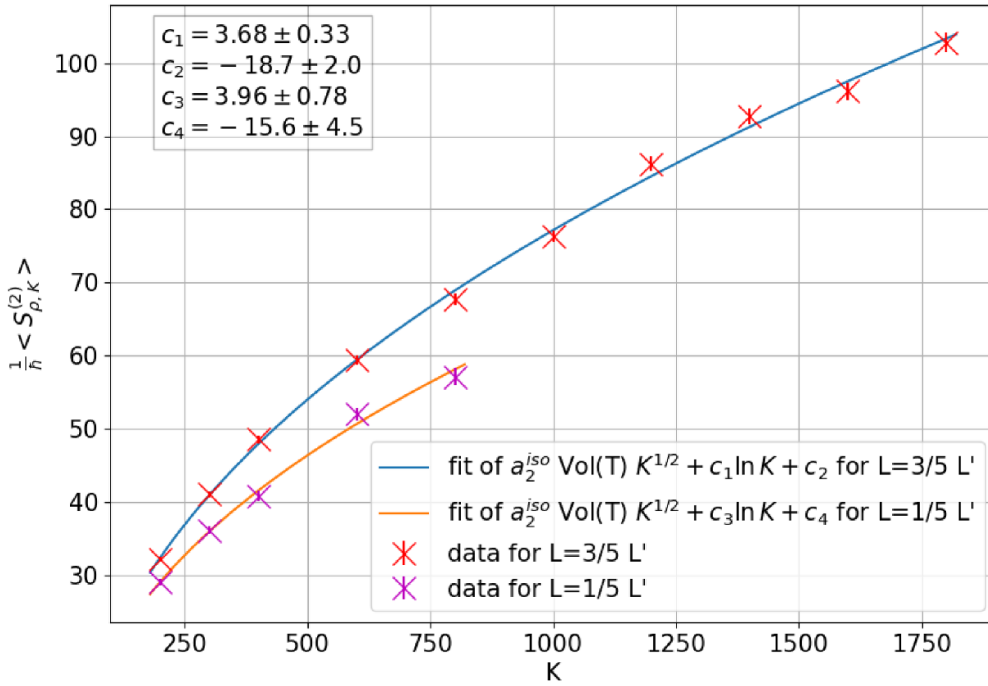


Figure 18. Sample mean of the action against K for square holes with lengths $L = \frac{3}{5}L'$ and $L = \frac{1}{5}L'$. $\text{Vol}(T) = 2(L + L')$ as before.

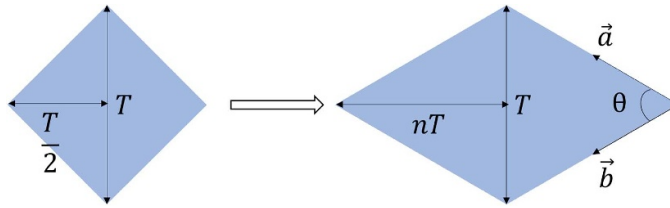


Figure 19. The $d = 2$ causal diamond (left) stretched to give a lozenge (right), where $n > \frac{1}{2}$. The vectors \vec{a} and \vec{b} are used to define the Lorentzian angle θ .

for stronger evidence we will need larger simulations and more knowledge of the subleading corrections.

7. Spacelike joints

7.1. The Lozenge

If we stretch the causal diamond so that its null boundaries become spacelike (shown in figure 19), we obtain a globally hyperbolic lozenge and according to conjecture 1, it should have the same mean action in the infinite limit as the diamond i.e. 2 for $d = 2$.

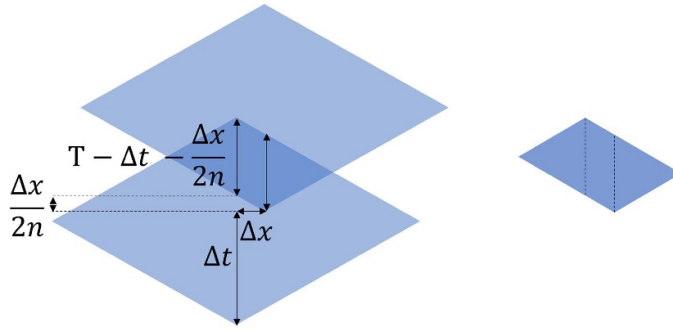


Figure 20. Left: showing how the volume of realisation (the shaded region) can be found from cloning. The length $\frac{\Delta x}{2n}$ is found using similar triangles. Right: showing how the volume of realisation can be broken into 2 identical triangles either side of a parallelogram.

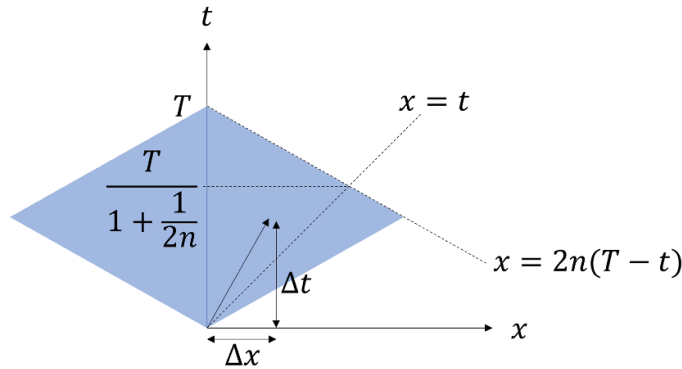


Figure 21. Showing the constraints on the defining vector $(\Delta t, \Delta x)$ for $\Delta x > 0$.

We used the weighted integral method to compute the mean action. The cloning is shown in figure 20, from which the volume of realisation is

$$a(\vec{c}) = 2 \times \frac{n}{2} \left(T - \Delta t - \frac{\Delta x}{2n} \right)^2 + \left(T - \Delta t - \frac{\Delta x}{2n} \right) \Delta x \tag{52}$$

where the first term is the area of the 2 triangles and the second term is the area of the parallelogram between them.

For the defining vector $(\Delta t, \Delta x)$ to define an interval, it must satisfy $|\Delta x| < \Delta t$.

Using figure 21 and the volume of realisation, the integral for X_ρ is

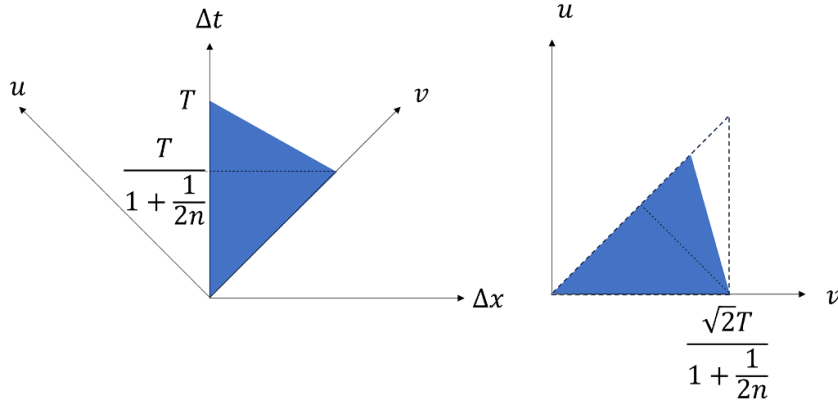


Figure 22. Converting the integration region from Cartesian (left) into null coordinates (right) and approximating the integral using the larger, dashed triangle.

$$\begin{aligned}
X_\rho = & 2 \int_0^{\frac{T}{1+\frac{1}{2n}}} d\Delta t \int_0^{\Delta t} d\Delta x \left[n \left(T - \Delta t - \frac{\Delta x}{2n} \right)^2 \right. \\
& \left. + \Delta x \left(T - \Delta t - \frac{\Delta x}{2n} \right) \right] e^{-\frac{\rho}{2}(\Delta t^2 - \Delta x^2)} \\
& + 2 \int_{\frac{T}{1+\frac{1}{2n}}}^T d\Delta t \int_0^{2n(T-\Delta t)} d\Delta x \left[n \left(T - \Delta t - \frac{\Delta x}{2n} \right)^2 \right. \\
& \left. + \Delta x \left(T - \Delta t - \frac{\Delta x}{2n} \right) \right] e^{-\frac{\rho}{2}(\Delta t^2 - \Delta x^2)}.
\end{aligned} \tag{53}$$

The factor of 2 accounts for the contribution from $\Delta x < 0$. To compute this integral, we change to u and v coordinates and make use of a similar approximation as in the infinite slab calculation. In this approximation, we again extend the region of integration to a larger triangle, shown in figure 22.

The expression for X_ρ becomes:

$$\begin{aligned}
X_\rho = & 2 \int_0^{\frac{\sqrt{2}T}{1+\frac{1}{2n}}} dv \int_0^v du \left(\frac{1}{2} n \left(2T^2 - 2\sqrt{2}T(u+v) + (u+v)^2 \right) \right. \\
& \left. - \frac{(u-v)^2}{8n} \right) e^{-\rho uv}.
\end{aligned} \tag{54}$$

Using equation (24) for the mean action in terms of X_ρ and the operator $\hat{\mathcal{O}}_2$ we find the limit is

$$\lim_{\rho \rightarrow \infty} \frac{1}{\hbar} \langle \mathcal{S}_\rho^{(2)}(M) \rangle = 2n + \frac{1}{2n}. \tag{55}$$

For $n = \frac{1}{2}$ we recover the correct value of 2 for the limiting mean action of the causal interval. For $n > \frac{1}{2}$, however, this result violates the original conjecture 1 for globally hyperbolic manifolds.

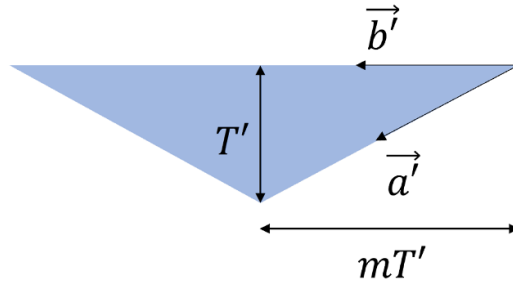


Figure 23. The spacelike triangle.

7.2. Lorentzian angle

We can generalise this result for different manifolds. If we assume that each joint of the lozenge contributes half of the action, we can state that:

$$\lim_{\rho \rightarrow \infty} \frac{1}{\hbar} \langle S_{\rho}^{(2)}(\text{joint}) \rangle = n + \frac{1}{4n}. \tag{56}$$

We can write this in terms of a Lorentzian angle θ , defined as [28]

$$\theta = \cosh^{-1} \left(\frac{\vec{a} \cdot \vec{b}}{|\vec{a}| |\vec{b}|} \right) \tag{57}$$

where \vec{a} (\vec{b}) is the tangent vector to the future (past) boundary at the joint as shown as in figure 19, $|\vec{a}| = |\sqrt{\vec{a} \cdot \vec{a}}|$ and $\vec{a} \cdot \vec{b} = -a_t b_t + a_x b_x$.

θ is Lorentz invariant and we conjecture that any joint with the same Lorentzian angle contributes the same amount to the mean action. From figure 19, we can see that $\vec{a} = \begin{pmatrix} \frac{T}{2} \\ -nT \end{pmatrix}$ and $\vec{b} = \begin{pmatrix} -\frac{T}{2} \\ -nT \end{pmatrix}$, giving

$$\theta = \cosh^{-1} \left(\frac{n^2 + \frac{1}{4}}{n^2 - \frac{1}{4}} \right). \tag{58}$$

This can be rearranged to give

$$n = \frac{1}{2} \sqrt{\frac{\cosh \theta + 1}{\cosh \theta - 1}} \tag{59}$$

and so we find

$$\lim_{\rho \rightarrow \infty} \frac{1}{\hbar} \langle S_{\rho}^{(2)}(\text{joint}) \rangle = \frac{1}{2} \left(\sqrt{\frac{\cosh \theta + 1}{\cosh \theta - 1}} + \sqrt{\frac{\cosh \theta - 1}{\cosh \theta + 1}} \right) = \coth \theta. \tag{60}$$

7.3. Spacelike triangle

To test the conjecture that the mean action depends only on Lorentzian angle as above, we now compute the mean action of a triangle with 3 spacelike sides, as shown in figure 23.

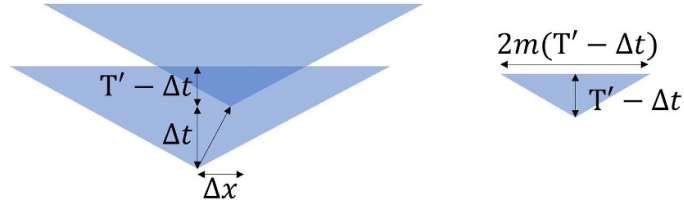


Figure 24. Left: cloning the triangle to find the volume of realisation. Right: the volume of realisation, where the base length is found using similar triangles.

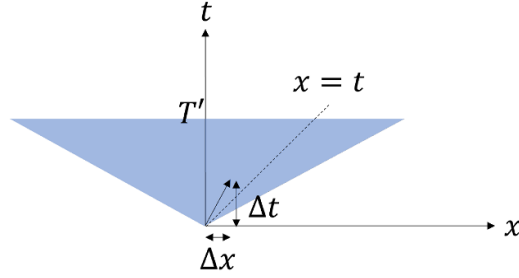


Figure 25. Showing the constraints on the defining vector, only considering $\Delta x > 0$.

Again, we find the volume of realisation by cloning, shown in figure 24. This gives the volume as:

$$a(\vec{c}) = m(T' - \Delta t)^2. \quad (61)$$

The limits can be found by considering the defining vector that will give a non-zero volume of realisation, shown in figure 25

Therefore

$$X_\rho = 2 \int_0^{T'} d\Delta t \int_0^{\Delta t} d\Delta x m (T' - \Delta t)^2 e^{-\frac{\rho}{2}(\Delta t^2 - \Delta x^2)}. \quad (62)$$

We again use null coordinates and the same approximation as before as shown in figure 26, giving:

$$X_\rho = 2 \int_0^{\sqrt{2}T'} dv \int_0^v du m \left(T' - \frac{u+v}{\sqrt{2}} \right)^2 e^{-\rho uv} \quad (63)$$

and hence find

$$\lim_{\rho \rightarrow \infty} \frac{1}{\hbar} \langle \mathcal{S}_\rho^{(2)}(\text{joint}) \rangle = m. \quad (64)$$

We now need to compute the Lorentzian angle for this joint. Taking $\vec{a}' = \begin{pmatrix} -T' \\ -mT' \end{pmatrix}$ and $\vec{b}' = \begin{pmatrix} 0 \\ -mT' \end{pmatrix}$ (from figure 23), we find that

$$\theta = \cosh^{-1} \left(\frac{m}{\sqrt{m^2 - 1}} \right). \quad (65)$$

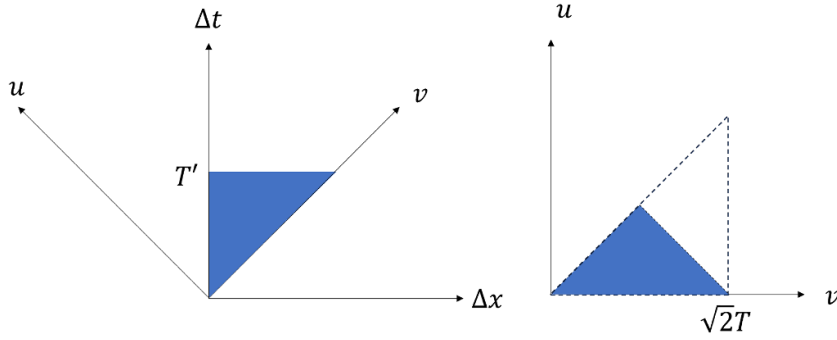


Figure 26. Converting the integration region from Cartesian (left) into null coordinates (right) and approximating the integral using the larger, dashed triangle.

By inverting this, the action is found to be:

$$\lim_{\rho \rightarrow \infty} \frac{1}{\hbar} \langle S_\rho^{(2)}(\text{joint}) \rangle = \frac{\cosh \theta}{\sqrt{\cosh^2 \theta - 1}} = \coth \theta. \quad (66)$$

As expected, this is the same result as found in the previous section. Therefore, we expect that this expression will hold for the joint of any globally hyperbolic shape for $d = 2$. We can rewrite the conjecture for globally hyperbolic manifolds in 2 dimensions as:

$$\lim_{\rho \rightarrow \infty} \frac{1}{\hbar} \langle S_\rho^{(2)}(M) \rangle = \int_M d^2x \sqrt{-g} \frac{R}{2} + \sum_i \coth \theta_i \quad (67)$$

where θ_i is the Lorentzian angle of joint i , and the sum is over all joints in the manifold. For a null joint, θ is infinite and so $\coth \theta$ will tend to 1. The sum will therefore count the number of points that make up the joint, i.e. the volume of the joint.

7.4. Higher dimensions

For $d = 3$ and higher, the joint is a co-dimension 2 spacelike submanifold. At any point on the joint the vector \vec{a} (\vec{b}) is tangent to the future (past) boundary and orthogonal to the joint. The Lorentzian angle θ of the joint at that point is defined by equation (57) and it can vary over the joint.

If λ denotes the point on the joint and $d\mu(\lambda)$ the $(d - 2)$ -volume measure of the joint at that point, then the new conjecture is:

$$\lim_{\rho \rightarrow \infty} \frac{1}{\hbar} \langle S_\rho^{(d)}(M) \rangle = \frac{1}{l_p^{d-2}} \int_M d^d x \sqrt{-g} \frac{R}{2} + \frac{1}{l_p^{d-2}} \int_J d\mu(\lambda) \coth(\theta(\lambda)). \quad (68)$$

where

$$\int_J d\mu(\lambda) = \text{Vol}_{d-2}(J). \quad (69)$$

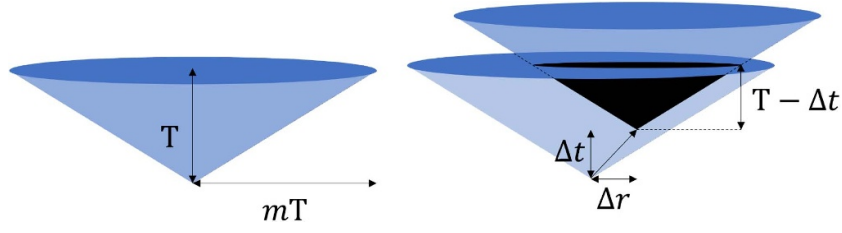


Figure 27. Left: the $d=3$ cone. Right: showing that the volume of realisation (the volume of the black cone) is equal to the volume of original cone scaled by $\left(\frac{T-\Delta t}{T}\right)^3$. This will be true in arbitrary dimensions (replacing 3 with d).

We can test this conjecture on a d dimensional cone where all the boundaries are spacelike. An example is the $d=3$ cone shown in figure 27. We use spherical coordinates. The volume of realisation is

$$a(\vec{c}) = \frac{T \pi^{\frac{d-1}{2}} (mT)^{d-1}}{d \Gamma\left(\frac{d+1}{2}\right)} \left(\frac{T-\Delta t}{T}\right)^d, \quad (70)$$

which is the volume of the manifold (the volume of a hypercone with height T and base radius mT), but scaled by a factor of $\left(\frac{T-\Delta t}{T}\right)^d$ according to figure 27.

Then, we obtain

$$\begin{aligned} X_\rho &= 2^{d-1} \int_0^T d\Delta t \int_0^{\Delta t} d\Delta r \prod_{i=0}^{d-3} \int_0^{\pi/2} d\Delta\phi_i \sin(\Delta\phi_i)^i \Delta r^{d-2} \\ &\times \frac{T \pi^{\frac{d-1}{2}} (mT)^{d-1}}{d \Gamma\left(\frac{d+1}{2}\right)} \left(\frac{T-\Delta t}{T}\right)^d e^{-\rho V_c} \end{aligned} \quad (71)$$

where V_c is given by equation (36). We use the null coordinates in equation (34) to obtain:

$$\begin{aligned} X_\rho &= 2^{d-1} \int_0^{\sqrt{2}T} dv \int_0^v du \prod_{i=0}^{d-3} \int_0^{\pi/2} d\Delta\phi_i \sin(\Delta\phi_i)^i \\ &\left(\frac{1}{\sqrt{2}}(v-u)\right)^{d-2} \frac{T \pi^{\frac{d-1}{2}} (mT)^{d-1}}{d \Gamma\left(\frac{d+1}{2}\right)} \left(\frac{T - \frac{1}{\sqrt{2}}(v+u)}{T}\right)^d e^{-\rho V_c} \end{aligned} \quad (72)$$

where we have again used our large ρ approximation, and integrated over the extended triangle region. We have checked for d up to 11 that the mean action gives

$$\begin{aligned} \lim_{\rho \rightarrow \infty} \frac{1}{\hbar} \langle S_\rho^{(d)}(M) \rangle &= \frac{1}{l_p^{d-2}} \frac{2\pi^{\frac{d-1}{2}}}{\Gamma\left(\frac{d-1}{2}\right)} (mT)^{d-2} m \\ &= \frac{1}{l_p^{d-2}} \text{Vol}_{d-2}(J) m \\ &= \frac{1}{l_p^{d-2}} \text{Vol}_{d-2}(J) \coth \theta. \end{aligned} \quad (73)$$

Since θ is constant around the joint in this case, this is consistent with the conjecture (68).

8. Discussion

Our analytical and numerical results in flat space support the conjectures in section 2.5. We also conjectured and provided evidence for the contribution of a spacelike hole to the continuum limit of the mean action (51). Testing the conjectures further is work for the future. We can, however, look forward to the implications that the conjectures might have for the sum-over-causal-sets qua path integral for quantum gravity. The starting point of the discussion is Feynman’s heuristic, quoted in the introduction, that the classical action principle emerges from the quantum mechanical path integral. The heuristic is an interplay between the magnitude of the action (in units of \hbar) and the number of histories that contribute essentially the same amount to the path integral, an interplay between action and measure. The heuristic assumes that we are working in a regime in which the magnitude of the action of all the histories in the path integral under consideration is large. In the context of causal set quantum gravity, that is the regime in which the cardinality N of the causal sets in the sum over histories (2) is large.

Our observable Universe is, as far as we can currently tell, without a timelike boundary or ‘edge of space’. We can ask why that is. We argue below that the action of causal sets that are typical sprinklings into spacetimes with a timelike boundary could lead to the suppression of such spacetimes in the gravitational path integral for cosmology, relative to spacetimes without timelike boundaries.

Suppose that the dimension of the causal set action in (2) $d = 4$ for definiteness. The action for $d = 4$ is given in equation (78) in appendix A and we state it here for easy reference:

$$\frac{1}{\hbar} S^{(4)}(C) = \zeta (N - N_1 + 9N_2 - 16N_3 + 8N_4). \quad (74)$$

where ζ is a fundamental constant of order 1. Let us consider a cosmological scenario in which the cardinality of the causal sets in the sum over histories is $N = 10^{240}$, the volume of the observable Universe in Planck units. Suppose, for the sake of the argument, that not only the KR orders but all non-manifoldlike causal sets are suppressed in the sum-over-histories [29], so that all we have left to consider in (2) are the manifoldlike causal sets, i.e. the typical sprinklings into Lorentzian spacetimes that vary only slowly on the fundamental scale. In other words we assume that there exists a *continuum regime* in causal set quantum gravity in which the continuum gravitational path integral (1) for spacetime of volume $V = 10^{240}$ in fundamental units makes sense at an effective level and is to be understood as being given fundamentally by a sum (2) over manifoldlike causal sets of cardinality $N = 10^{240}$. Essentially what we are assuming here is that the (causal set version of the) cosmological constant problem has been solved.

In the Feynmannian heuristic the contribution to the gravitational path integral (1) of a manifold (M, g) is determined by the measure of the neighbourhood of (M, g) over which the action, in units of \hbar , changes by an amount much smaller than one. A neighbourhood of (M, g) in (1) is an approximate continuum concept and corresponds in the fundamental theory to some neighbourhood of a typical sprinkling C into (M, g) in the set of manifoldlike causal sets of cardinality N . Saying that the action should vary only a little over the continuum neighbourhood of (M, g) means that the action should vary only a little over the causal sets in the corresponding neighbourhood of C .

If the dimension d' of (M, g) does not equal the dimension-parameter $d = 4$ in the causal set action in (2), then the action (74) of the sprinkled C will not enjoy the cancellation between its summands that results in the conjectured values of the action in section 2.5 and the order of magnitude of the action of C will be the order of magnitude of the dominant summand.

For an idea of what this order of magnitude is, for a causal interval in dimension $d' > 2$ the number of links N_1 in a typical sprinkling is of order $N^{2-2/d'}$ and for $d' = 2$ the number of links N_1 in a typical sprinkling is of order $N \log N$ [30]. A small change in C that changes each summand by a few will change the action by an amount of order 1. We expect therefore that there is essentially no neighbourhood of C in the set of manifoldlike causal sets over which the action varies by an amount $\ll 1$. In the effective continuum path integral this translates into the suppression of spacetimes with dimension not equal to 4 relative to spacetimes with dimension equal to 4.

We are then left, in the sum over causal sets, with the typical sprinklings into 4-dimensional spacetimes. This is the scenario to which our conjectures apply. We will ignore the fluctuations and assume that each causal set has an action given by the mean over sprinklings and further assume that the density of sprinkling $\rho = l^{-4}$ is high enough that the action is close to the limiting mean value. In this effective 4-dimensional continuum regime the constant ζ in the fundamental action is revealed to equal

$$\zeta = \frac{4}{\sqrt{6}} \left(\frac{l}{l_p} \right)^2, \tag{75}$$

where l_p is the 4-dimensional Planck length $l_p = \sqrt{8\pi G\hbar}$. Since ζ is a constant of order 1, our assumptions about the existence of the 4-dimensional continuum regime go hand in hand with the expectation that the fundamental discreteness length l is of order the Planck length l_p .

We can compare the actions $S(C_{\text{no edge}})$ and $S(C_{\text{edge}})$ of causal sets sprinkled into realistic cosmological spacetimes $M_{\text{no edge}}$ without a timelike or null boundary and M_{edge} with a timelike boundary, respectively. Our conjecture implies

$$\begin{aligned} \frac{1}{\hbar} S(C_{\text{no edge}}) &\approx \frac{1}{l_p^2} \int \sqrt{-g} d^4x \frac{R}{2} \sim \frac{V_4}{l_p^2} \Lambda \\ &\sim 10^{240} 10^{-120} \sim 10^{120} \end{aligned}$$

where V_4 is the spacetime volume of the Universe. If a manifold (M, g) has a timelike boundary our conjecture implies that the action of C tends, in the limit $l \rightarrow 0$, to the timelike boundary term. Physically, however, in causal set theory l the fundamental length is not zero but finite and in $S(C_{\text{edge}})$ for finite l there are competing terms, one of which is the EH term of the same order of magnitude as the above. The other is the timelike boundary term

$$\text{timelike boundary term of } \frac{1}{\hbar} S(C_{\text{edge}}) \sim \frac{1}{l_p^2} \frac{1}{l} V_3 \sim \frac{V_3}{l_p^3}.$$

If the timelike boundary is an edge of space of cosmological scale then its volume V_3 is of order $\frac{V_3}{l_p^3} \sim 10^{180}$ which dominates the EH term and so

$$\frac{1}{\hbar} S(C_{\text{edge}}) \sim 10^{180}.$$

Now we have an indication of a mechanism for suppression of spacetime M_{edge} compared to $M_{\text{no edge}}$. The large ratio of the magnitudes of their actions indicates that the measure of the neighbourhood of C_{edge} over which the action is approximately constant is much smaller than that of $C_{\text{no edge}}$, leading to the suppression of M_{edge} in the gravitational path integral.

The preceding argument is a rough sketch in which many issues are ignored¹¹. Not the least of these is the question of fluctuations around the mean of the causal set action and their implications for the sum-over-histories [31]. It may be that the action in the sum-over-causal sets should be replaced by the smeared form of the action, which we used in this article as a device in our simulations exactly because its fluctuations are small for large N . In the meantime, the work in this article can be extended in many ways. We have already mentioned larger simulations and gaining more knowledge of the finite density and finite ϵ corrections. The conjectures should be tested on manifolds in curved spacetime, and the low curvature regime would be an obvious place to start [22, 25].

Ultimately, if quantum gravity is a theory with no free parameters, one must hope that even the dimension of spacetime will emerge from the fundamental theory and not have to be entered by hand into the sum-over-histories for causal sets. One must hope then that the sum-over-histories given in (2) is itself an effective theory that arises from a yet more fundamental dynamics. One proposal for such dynamics is the class of sequential growth models [3–5] which hold the potential to be models of self-tuning universes. In such universes, what we now treat as fundamental constants such as $d = 4$ arise through a process of ‘cosmic renormalisation’ as cosmic epochs with different effective parameters succeed one another in an unceasing process [32–34].

Data availability statement

The data that support the findings of this study will be openly available following an embargo at the following URL/DOI: <https://github.com/RogerLiux/Timelike-boundary-and-corner-terms-in-the-causal-set-action.git>.

Acknowledgment

We thank Josh Chevalier for useful discussions. FD is supported in part by STFC Grant ST/ST/X000575/1 and by STFC Grant ST/W006537/1. Research at Perimeter Institute is supported by the Government of Canada through Industry Canada and by the Province of Ontario through the Ministry of Economic Development and Innovation.

Appendix A. Causal set actions for specific dimensions

The explicit forms of equation (3), as examples, for $d = 2, 3, 4$ are

$$\frac{1}{\hbar} S^{(2)}(\mathcal{C}) = 2(N - 2N_1 + 4N_2 - 2N_3), \quad (76)$$

$$\frac{1}{\hbar} S^{(3)}(\mathcal{C}) = \frac{1}{\Gamma(\frac{5}{3})} \left(\frac{\pi}{3\sqrt{2}} \right)^{\frac{2}{3}} \frac{l}{l_p} \left(N - N_1 + \frac{27}{8}N_2 - \frac{9}{4}N_3 \right), \quad (77)$$

$$\frac{1}{\hbar} S^{(4)}(\mathcal{C}) = \frac{4}{\sqrt{6}} \left(\frac{l}{l_p} \right)^2 (N - N_1 + 9N_2 - 16N_3 + 8N_4). \quad (78)$$

¹¹ One case that is being ignored is that of perhaps the most studied spacetime with a timelike boundary, Anti-De Sitter space. Causal intervals in AdS that intersect the boundary are of infinite volume and so causal sets that are sprinkled in AdS will not be locally finite. It is for future work to determine if the axioms of causal set theory can be modified to accommodate AdS.

Their smeared versions, the explicit forms of equation (16) for $d = 2, 3, 4$ are

$$\frac{1}{\hbar} S_\epsilon^{(2)}(\mathcal{C}) = 2 \left(\epsilon N - 2\epsilon^2 \sum_{x \in \mathcal{C}} \sum_{y \prec x} f_2(n(x, y), \epsilon) \right) \quad (79)$$

where

$$f_2(n, \epsilon) = (1 - \epsilon)^n - 2n\epsilon(1 - \epsilon)^{n-1} + \binom{n}{2} \epsilon^2 (1 - \epsilon)^{n-2}, \quad (80)$$

$$\frac{1}{\hbar} S_\epsilon^{(3)}(\mathcal{C}) = \frac{1}{\Gamma(\frac{5}{3})} \left(\frac{\pi}{3\sqrt{2}} \right)^{\frac{2}{3}} \frac{l}{l_p} \left(\epsilon^{2/3} N - \epsilon^{5/3} \sum_{x \in \mathcal{C}} \sum_{y \prec x} f_3(n(x, y), \epsilon) \right) \quad (81)$$

where

$$f_3(n, \epsilon) = (1 - \epsilon)^n - \frac{27}{8} n\epsilon(1 - \epsilon)^{n-1} + \frac{9}{4} \binom{n}{2} \epsilon^2 (1 - \epsilon)^{n-2}, \quad (82)$$

$$\frac{1}{\hbar} S_\epsilon^{(4)}(\mathcal{C}) = \frac{4}{\sqrt{6}} \left(\frac{l}{l_p} \right)^2 \left(\epsilon^{1/2} N - \epsilon^{3/2} \sum_{x \in \mathcal{C}} \sum_{y \prec x} f_4(n(x, y), \epsilon) \right) \quad (83)$$

where

$$f_4(n, \epsilon) = (1 - \epsilon)^n - 9n\epsilon(1 - \epsilon)^{n-1} + 16 \binom{n}{2} \epsilon^2 (1 - \epsilon)^{n-2} - 8 \binom{n}{3} \epsilon^3 (1 - \epsilon)^{n-3} \quad (84)$$

which we used in our simulations.

Appendix B. The cross terms in the $d = 2$ diamond

In this appendix we verify the result from section 3.1 that the $d = 2$ joint term for the corner is not present at subleading order in (24). A causal diamond has a mean action of 2 in the limit of infinite ρ . This is interpreted according to conjecture 1 as being the contribution of the 2 points, S^0 , of the joint. We can investigate the result for the triangle by considering it as one of two isometric halves of the diamond which gives us a chance to calculate an example of the bi-action defined above. Due to the bilocal nature of the action, we cannot simply sum the action of the left triangle and the right triangle to obtain the action of the diamond. Instead equation (9) must be used:

$$\langle S_{\text{diamond}} \rangle = \langle S_L \rangle + \langle S_R \rangle + \langle S_{L,R} \rangle + \langle S_{R,L} \rangle \quad (85)$$

where L refers to the left triangle and R the right. $\langle S_{L,R} \rangle$ is the mean action calculated by only considering intervals which begin in the right triangle and end in the left triangle. Similarly $\langle S_{R,L} \rangle$, considers intervals which begin in the left and end in the right. To find $\langle S_{R,L} \rangle$, cloning can again be used. We clone the left hand region and displace it by the defining vector (u, v) . The volume of realisation is then given by the overlapping area between the cloned left hand region and the right hand region.

From figure 28, the overlapping area can be seen to be $(L - v)(v - u)$. In order for these two regions to intersect, $L > v > u$. Therefore, X_ρ is given by

$$\begin{aligned} X_\rho &= \int_0^L du \int_u^L dv (L - v)(v - u) e^{-\rho uv} \\ &= \frac{-2\sqrt{\pi} L \sqrt{\rho} \text{Erf}(L\sqrt{\rho}) - \text{Ei}(-L^2\rho) + L^2\rho - 2e^{-L^2\rho} + 2\log(L) + \log(\rho) + \gamma + 2}{2\rho^2}. \end{aligned} \quad (86)$$

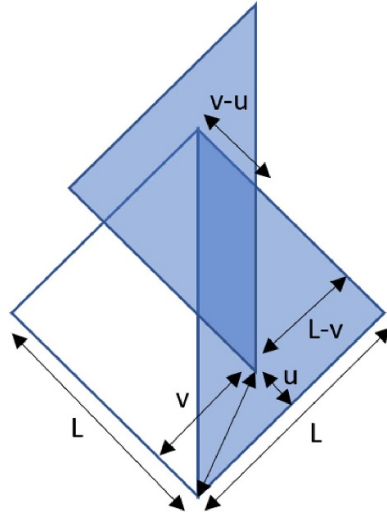


Figure 28. The volume of realisation (shaded) for the cross terms.

The action can then be computed:

$$\frac{1}{\hbar} \langle \mathbf{S}_{L,R} \rangle = -4\rho^2 \hat{O}_2 X_\rho = -\frac{1}{2} \sqrt{\pi} L \sqrt{\rho} \text{Erf}(L\sqrt{\rho}) - e^{-L^2\rho} + 1. \quad (87)$$

From symmetry, $\langle \mathbf{S}_{L,R} \rangle = \langle \mathbf{S}_{R,L} \rangle$ and $\langle \mathbf{S}_L \rangle = \langle \mathbf{S}_R \rangle$. Therefore

$$\begin{aligned} \frac{1}{\hbar} \langle \mathbf{S}_{\text{diamond}} \rangle &= 2 \left(\frac{1}{2} \sqrt{\pi} L \sqrt{\rho} \text{Erf}(L\sqrt{\rho}) \right) + 2 \left(-\frac{1}{2} \sqrt{\pi} L \sqrt{\rho} \text{Erf}(L\sqrt{\rho}) - e^{-L^2\rho} + 1 \right) \\ &= 2 \left(1 - e^{-L^2\rho} \right) \end{aligned} \quad (88)$$

which is the known result [24].

Appendix C. $d = 2$ timelike-spacelike (t-s) corners in the embedded regime

C.1. Half lozenge

To find the contribution from the intersection of timelike and spacelike boundaries, we can consider the action of half of the lozenge, shown in figure 29. We want to conclude that due to the presence of the timelike boundary, any contributions from these corners will be dominated by the $\rho^{\frac{1}{2}}$ term, so they are not of great importance.

The volume of realisation is

$$\frac{1}{2} n \left(T - \Delta t - \frac{\Delta x}{2n} \right)^2 \quad (89)$$

which can be seen from figure 30.

The limits of integration are the same as for the lozenge in section 7.1. Therefore

$$X_\rho = 2 \int_0^{\frac{\sqrt{2}T}{1+\frac{1}{2n}}} dv \int_0^v du \frac{e^{-\rho uv} \left(\sqrt{2}((2n-1)u + 2nv + v) - 4nT \right)^2}{32n}. \quad (90)$$

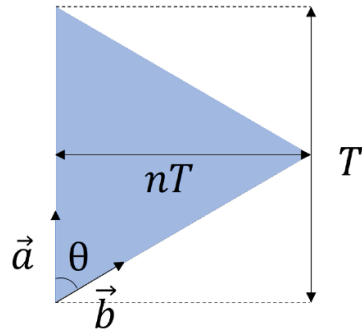


Figure 29. Half of the lozenge. The vectors are used to define the Lorentzian angle of the timelike-spacelike corner.

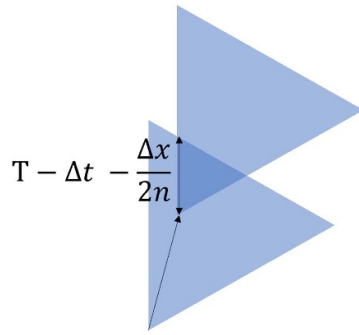


Figure 30. Finding the volume of realisation.

This gives

$$\begin{aligned} \frac{1}{\hbar} \langle S_\rho^{(2)}(M) \rangle &= \rho n T^2 - 4\rho^2 \hat{O}_2 X_\rho \\ &= n - \frac{1}{4n} + \frac{1}{2} \sqrt{\frac{\pi}{2}} \sqrt{\rho} T + \mathcal{O}\left(\left(\frac{1}{\rho}\right)^1\right) \end{aligned} \tag{91}$$

This has the expected $\sqrt{\rho}$ contribution from the timelike boundary. Since we know that the joint contributes $n + \frac{1}{4n}$ (from section 7.2), we expect that the 2 timelike-spacelike corners contribute $-\frac{1}{2n}$. Therefore

$$\lim_{\rho \rightarrow \infty} \frac{1}{\hbar} \langle S_\rho^{(2)}(\text{t-s corner}) \rangle = -\frac{1}{4n}. \tag{92}$$

When $n = \frac{1}{2}$, the null case, this gives $-\frac{1}{2}$ and so is consistent with section 3.1.

C.2. Lorentzian angle

According to the definition of Lorentzian Angle θ in [28] for a timelike vector \vec{a} and a spacelike vector \vec{b} ,

$$\cosh \theta = -i \frac{\vec{a} \cdot \vec{b}}{||\vec{a}|| ||\vec{b}||}, \tag{93}$$

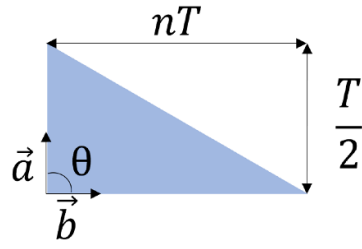


Figure 31. A quarter of the lozenge. This has 2 different spacelike-timelike corners.

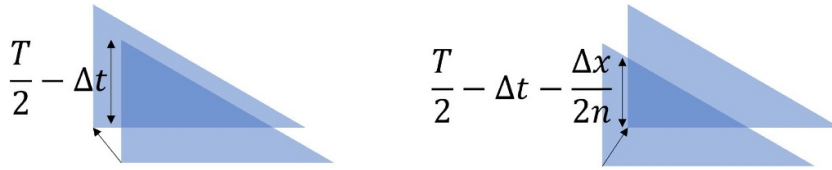


Figure 32. Finding the volume of realisation.

where $||\vec{a}||$ is the absolute value of $|\vec{a}|$. From section C.1, we can find

$$\cosh \theta = \frac{i}{2\sqrt{n^2 - 1/4}}, \text{ for } \vec{a} = \begin{pmatrix} T \\ 0 \end{pmatrix}, \vec{b} = \begin{pmatrix} T/2 \\ nT \end{pmatrix} \tag{94}$$

where \vec{a} and \vec{b} come from section C.1. This can be rearranged to

$$n = \frac{\sqrt{\cosh^2 \theta - 1}}{2 \cosh \theta} = \frac{1}{2} \tanh \theta \tag{95}$$

so we can substitute this result into equation (92) which gives

$$\lim_{\rho \rightarrow \infty} \frac{1}{\hbar} \langle S_\rho^{(2)}(\text{t-s corner}) \rangle = -\frac{1}{4n} = -\frac{1}{2} \coth \theta. \tag{96}$$

C.3. Quarter lozenge

To check this result for different timelike-spacelike corners, we can compute the action of the quarter lozenge, shown in figure 31.

For $\Delta x > 0$, this has volume of realisation

$$n \left(\frac{T}{2} - \Delta t - \frac{\Delta x}{2n} \right)^2 \tag{97}$$

whereas for $\Delta x < 0$, the volume of realisation is

$$n \left(\frac{T}{2} - \Delta t \right)^2 \tag{98}$$

as can be seen from figure 32.

To find the limits, we must consider when the defining vector gives a non-zero volume of resolution. This can be seen in figure 33.

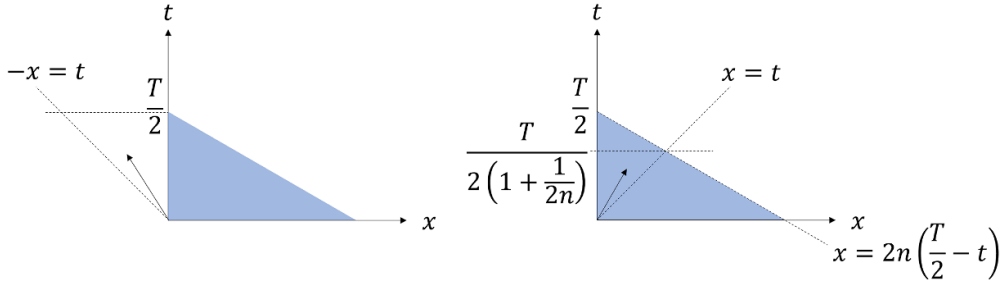


Figure 33. The limits of the integral can be found by considering the area over which the defining vector can range. This is different for $\Delta x < 0$ (left) and $\Delta x > 0$ (right).

Converting these limits to (u, v) coordinates and using the approximation, we find

$$X_\rho = \int_0^{\frac{\sqrt{2}T}{2(1+\frac{1}{2n})}} dv \int_0^v du \frac{e^{-\rho uv} \left(\sqrt{2}((2n-1)u + 2nv + v) - 2nT \right)^2}{16n} \quad (99)$$

$$+ \int_0^{\frac{\sqrt{2}}{2}T} dv \int_0^v du \frac{1}{4} n \left(T - \sqrt{2}(u+v) \right)^2 e^{-\rho uv}$$

and so

$$\begin{aligned} \frac{1}{\hbar} \langle \mathbf{S}_\rho^{(2)}(M) \rangle &= \frac{1}{2} \rho n T^2 - 4\rho^2 \hat{\mathcal{O}}_2 X_\rho \\ &= 2n - \frac{1}{4n} + \frac{1}{4} \sqrt{\frac{\pi}{2}} \sqrt{\rho} T + \mathcal{O} \left(\left(\frac{1}{\rho} \right)^1 \right). \end{aligned} \quad (100)$$

Again, there is the expected timelike boundary contribution. From section C.1, the upper t-s corner should contribute $-\frac{1}{4n}$. We also know from section 7.3 that the joint will contribute $2n$ (setting $m = 2n$). Therefore the lower s-t corner should contribute 0. This is consistent with our conjecture in equation (96). From figure 31, we can work out

$$\cosh \theta = 0, \text{ for } \vec{a} = \begin{pmatrix} T \\ 0 \end{pmatrix}, \vec{b} = \begin{pmatrix} 0 \\ nT \end{pmatrix} \quad (101)$$

so it is simple to see that the contribution to the action from this corner is indeed zero.

Appendix D. Argument for assumption

Region 2 touches the v -axis at $(0, v_0)$ in u, v coordinates (where $v_0 = \sqrt{2}T$ for the infinite slab case). $X_\rho^{(2)}$ therefore may contribute non-exponentially suppressed terms to the action.

Recall from equation (8) that

$$\frac{1}{\hbar} \langle \mathbf{S}_\rho^{(d)}(M) \rangle = -\alpha_d \left(\frac{l}{l_p} \right)^{d-2} \left(\rho V + \frac{\beta_d}{\alpha_d} \rho^2 \hat{\mathcal{O}}_d X_\rho \right). \quad (102)$$

Our aim is to show that $l^{d-2} \rho^2 \hat{\mathcal{O}}_d X_\rho^{(2)} = \rho^{1+2/d} \hat{\mathcal{O}}_d X_\rho^{(2)}$ does not contribute to $\mathcal{O}(\rho^{1/d})$, the leading order of the action, which is the conjecture term.

Firstly, we numerically calculate $\rho^{1+2/d} \hat{\mathcal{O}}_d X_\rho^{(2)}$ for $d = 2, 3, 4$, and plotted the results for large ρ values in figure 34.

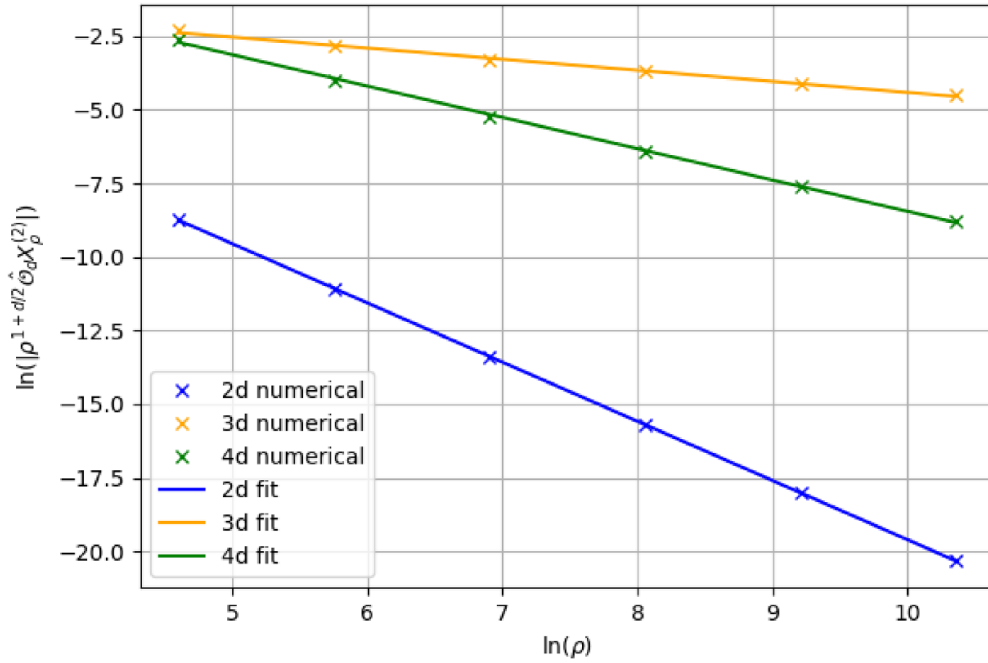


Figure 34. Plot of numerically integrated values $\rho^{1+2/d} \hat{O}_d X_\rho^{(2)}$ against ρ on a log scale. The data is fitted for each dimension with a straight line.

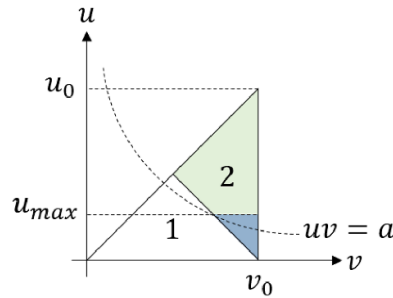


Figure 35. Region 1 here is the shaded region in figure 5(right). The shaded area in blue is labelled A(down), and the shaded area in green is labelled A(up).

By fitting each dimension with a straight line $\ln(|\rho^{1+2/d} \hat{O}_d X_\rho^{(2)}|) = c_1 \ln(\rho) + c_2$ on a log scale, we obtain ρ^{c_1} as the leading order contribution to the action from region 2. For $d=2$, $c_1 = -2.01 \pm 0.04, c_2 = 0.51 \pm 0.03$; for $d=3$, $c_1 = -0.38 \pm 0.01, c_2 = 0.65 \pm 0.08$; for $d=4$, $c_1 = -1.06 \pm 0.02, c_2 = 2.2 \pm 0.1$. It is noted that $c_1 < 1/d$ for these dimensions, so $l^{d-2} \rho^2 \hat{O}_d X_\rho^{(2)}$ does not interfere with the conjecture term in these dimensions. These c_1 values are also close to $-2, -1/3$, and -1 , which c_1 may approach as $\rho \rightarrow \infty$.

For an analytical argument, we can define

$$g(u, v) = \rho^{1+2/d} \hat{O}_d \left(f(u, v) e^{-c(d)\rho(uv)^{d/2}} \right) \tag{103}$$

where

$$f(u, v) = \frac{(2\pi)^{\frac{d}{2}-2} (v-u)^{d-2} \left(\sqrt{2}(u+v) - 2T \right) \left(2\pi L\Gamma\left(\frac{d}{2}\right) + \sqrt{2\pi}\Gamma\left(\frac{d-1}{2}\right) (u-v) \right)}{\Gamma(d-1)} \quad (104)$$

from equation (35). Therefore

$$\rho^{1+2/d} \hat{O}_d X_\rho^{(2)} = \int_{-\infty}^{\infty} dx_2 \dots \int_{-\infty}^{\infty} dx_{d-1} \int_{\frac{T}{\sqrt{2}}}^{\sqrt{2}T} dv \int_{\sqrt{2}T-v}^v du g(u, v). \quad (105)$$

The strategy is to define a parameter $a = uv$, where $\rho a^{d/2} \gg 1$. Region 2 is then divided into 2 regions, with the area named $A(\text{up})$ and $A(\text{down})$ shown in figure 35. We will separately argue that the contribution to the integral from $A(\text{up})$ and $A(\text{down})$ does not contribute to the conjecture term.

D.1. Integration in $A(\text{up})$

We first argue that the contribution to the integral from $A(\text{up})$ can be arbitrarily small for a choice of large ρ . We define g_{\max} to be the maximum value of $g(u, v)$ in $A(\text{up})$. $A(\text{up})$ lies above the hyperbola, so $uv > a$ in this region. Therefore,

$$e^{-c(d)\rho(uv)^{d/2}} \leq e^{-c(d)\rho a^{d/2}}, \quad (106)$$

hence

$$\int_{-\infty}^{\infty} dx_2 \dots \int_{-\infty}^{\infty} dx_{d-1} \int \int_{A(\text{up})} dudv g(u, v) \leq g_{\max} A(\text{up}) \leq g_{\max} A(2). \quad (107)$$

where $A(2)$ is the area of region 2. Since $A(2)$ is finite, and g_{\max} can be arbitrarily small for large enough ρ , it is always possible to find

$$\int_{-\infty}^{\infty} dx_2 \dots \int_{-\infty}^{\infty} dx_{d-1} \int \int_{A(\text{up})} dudv g(u, v) < \epsilon, \quad (108)$$

for any ϵ , hence this integral does not contribute to the leading order of the action (which diverges) in the large ρ limit.

D.2. Integration in $A(\text{down})$

To argue that

$$\int_{-\infty}^{\infty} dx_2 \dots \int_{-\infty}^{\infty} dx_{d-1} \int \int_{A(\text{down})} dudv g(u, v) \quad (109)$$

also does not contribute to the leading order of action, we choose

$$a^{\frac{d}{2}} = \rho^{-1+\alpha}, \text{ where } 0 < \alpha < 1. \quad (110)$$

From this choice, as ρ increases, $a = uv$ becomes closer to the $u = 0$ line. The argument is to take a large ρ such that v is close to v_0 and so we can treat $g(u, v)$ as $g(u, v_0)$. We first notice that the operator \hat{O}_d is designed such that

$$\hat{O}_d \left(\rho^{-2/d} \right) = \hat{O}_d \left(\rho^{-4/d} \right) = \dots = \hat{O}_d \left(\rho^{-(d+2)/d} \right) = 0 \quad (111)$$

for even d and

$$\hat{O}_d \left(\rho^{-2/d} \right) = \hat{O}_d \left(\rho^{-4/d} \right) = \dots = \hat{O}_d \left(\rho^{-(d+1)/d} \right) = 0 \quad (112)$$

for odd d [8, 27]. Then we rewrite

$$\begin{aligned} \int_{-\infty}^{\infty} dx_2 \dots \int_{-\infty}^{\infty} dx_{d-1} \int \int_{A(\text{down})} dudv g(u, v) &\sim \int_{-\infty}^{\infty} dx_2 \dots \int_{-\infty}^{\infty} dx_{d-1} \int_0^{u_{\max}} du g(u, v_0) \\ &= \rho^{1+2/d} \hat{\mathcal{O}}_d \left(\int_{-\infty}^{\infty} dx_2 \dots \int_{-\infty}^{\infty} dx_{d-1} \int_0^{u_{\max}} du f(u, v_0) e^{-c(d)\rho(uv_0)^{d/2}} \right). \end{aligned} \quad (113)$$

We note that $f(u, v_0)$ can be written in the form of a polynomial of u , with u^n where $n \in \mathcal{N}$. The integral

$$\int_0^{u_{\max}} du f(u, v_0) e^{-c(d)\rho(uv_0)^{d/2}} \quad (114)$$

can then only produce polynomials of ρ^m , where $m = -2/d, -4/d, \dots$ for $u_{\max} > 0$. Limited by equation (111) and (112), the first non-vanishing orders according to $\hat{\mathcal{O}}_d$ are $\rho^{-(d+4)/d}$ for even d , and $\rho^{-(d+3)/d}$ for odd d . Together with the $\rho^{1+2/d}$ factor outside of the operator, the integral in $A(\text{down})$ should *at most* be of order $\rho^{-2/d}$ for even d and $\rho^{-1/d}$ for odd d , hence should always be smaller than the conjecture term. This agrees with the numerical work in figure 34.

ORCID iDs

Fay Dowker  0000-0002-6652-1058

Roger Liu  0009-0000-4396-7914

Daniel Lloyd-Jones  0009-0005-2005-1627

References

- [1] Surya S 2012 Evidence for a phase transition in 2D causal set quantum gravity *Class. Quantum Grav.* **29** 132001
- [2] Glaser L, O'Connor D and Surya S 2018 Finite size scaling in 2D causal set quantum gravity *Class. Quantum Grav.* **35** 045006
- [3] Rideout D P and Sorkin R D 2000 A Classical sequential growth dynamics for causal sets *Phys. Rev. D* **61** 024002
- [4] Dowker F, Johnston S and Surya S 2010 On extending the Quantum Measure *J. Phys. A: Math. Theor.* **43** 505305
- [5] Surya S and Zalel S 2020 A criterion for covariance in complex sequential growth models *Class. Quantum Grav.* **37** 195030
- [6] Benincasa D M and Dowker F 2010 The scalar curvature of a causal set *Phys. Rev. Lett.* **104** 181301
- [7] Benincasa D 2013 The action of a causal set *PhD Thesis* (Imperial College) (available at: <https://spiral.imperial.ac.uk/bitstream/10044/1/14170/1/Benincasa-DMT-2013-PhD-Thesis.pdf>)
- [8] Dowker F and Glaser L 2013 Causal set d'Alembertians for various dimensions *Class. Quantum Grav.* **30** 195016
- [9] Glaser L 2014 A closed form expression for the causal set d'Alembertian *Class. Quantum Grav.* **31** 095007
- [10] Bombelli L, Lee J, Meyer D and Sorkin R D 1987 Space-time as a causal set *Phys. Rev. Lett.* **59** 521–4
- [11] Kleitman D and Rothschild B 1970 The number of finite topologies *Proc. Am. Math. Soc.* **25** 276–82
- [12] Kleitman D and Rothschild B 1975 Asymptotic enumeration of partial orders on a finite set *Trans. Am. Math. Soc.* **205** 205–20
- [13] Loomis S and Carlip S 2018 Suppression of non-manifold-like sets in the causal set path integral *Class. Quantum Grav.* **35** 024002
- [14] Mathur A, Singh A A and Surya S 2021 Entropy and the link action in the causal set path-sum *Class. Quantum Grav.* **38** 045017

- [15] Cunningham W J and Surya S 2020 Dimensionally restricted causal set quantum gravity: examples in two and three dimensions *Class. Quantum Grav.* **37** 054002
- [16] Carlip P, Carlip S and Surya S 2024 The Einstein–Hilbert action for entropically dominant causal sets *Class. Quantum Grav.* **41** 06
- [17] Feynman R P, Leighton R B and Sands M 1964 chapter 19: The principle of least action *The Feynman Lectures on Physics vol. II*
- [18] Dowker F and Butterfield J 2024 Recovering general relativity from a planck scale discrete theory of quantum gravity *Phil. Phys.* **2** 5
- [19] Saravani M and Aslanbeigi S 2014 On the causal set-continuum correspondence *Class. Quantum Grav.* **31** 205013
- [20] Surya S 2019 The causal set approach to quantum gravity *Living Rev. Relativ.* **22** 1
- [21] Butterfield J and Dowker F 2024 Recovering general relativity from a planck scale discrete theory of quantum gravity *Philos. Phys.* **2** 5
- [22] Dowker F 2020 Boundary contributions in the causal set action *Class. Quantum Grav.* **38** 075018
- [23] Chevalier J 2023 The discrete causal action and holes in spacetime *MSc Dissertation* (Imperial College London, Department of Physics) (available at: www.imperial.ac.uk/media/imperial-college/research-centres-and-groups/theoretical-physics/msc/dissertations/2023/Joshua-Chevalier-Dissertation.pdf)
- [24] Buck M, Dowker F, Jubb I and Surya S 2015 Boundary terms for causal sets *Class. Quantum Grav.* **32** 205004
- [25] Machet L and Wang J 2020 On the continuum limit of benincasa–dowker–glaser causal set action *Class. Quantum Grav.* **38** 015010
- [26] Benincasa D M, Dowker F and Schmitzer B 2011 The random discrete action for 2-dimensional spacetime *Class. Quantum Grav.* **28** 105018
- [27] Sorkin R D 2006 Does locality fail at intermediate length-scales? *Approaches to Quantum Gravity: Towards a New Understanding of Space and Time*, Ed D Oriti (Cambridge: Cambridge University Press)
- [28] Sorkin R D 2019 Lorentzian angles and trigonometry including lightlike vectors *Preprint* (arXiv:1908.10022)
- [29] Carlip S 2024 Causal sets and an emerging continuum (arXiv:2405.14059)
- [30] Glaser L and Surya S 2013 Towards a definition of locality in a manifoldlike causal set *Phys. Rev. D* **88** 124026
- [31] Moradi H, Yazdi Y K and Zilhão M 2024 Fluctuations and correlations in causal set theory (arXiv:2407.03395)
- [32] Sorkin R D 2000 Indications of causal set cosmology *Int. J. Theor. Phys.* **39** 1731–6
- [33] Martin X, O’Connor D, Rideout D P and Sorkin R D 2001 On the ‘renormalization’ transformations induced by cycles of expansion and contraction in causal set cosmology *Phys. Rev. D* **63** 084026
- [34] Dowker F and Zalel S 2023 Observables for cyclic causal set cosmologies *Class. Quantum Grav.* **40** 155015